Utrecht University

Graduate school of natural sciences

Institute for theoretical physics

Kerr black hole superradiance and gravitational lensing as a measure of ultralight bosons mass

Gastón Creci Keinbaum

June 2019

Master's thesis

under the supervision of

Prof. Dr. Stefan Vandoren

Utrecht University

Abstract

The effects of Kerr BH superradiance alongside ultralight boson fields has been poorly studied within electromagnetic radiation. Motivated by the Event Horizon Telescope results, we explore the observational implications using gravitational lensing. In order to do so, we review some key concepts like Detweiler's approximation and gravitational lensing. Later, we provide a fitted formula for the spin evolution and for measuring the spin of a Kerr black hole in terms of the shadow for an equatorial observer. We find that the spindown and mass change due to superradiance instability can be observable by changes in the black hole shadow, leaving a characteristic imprint and therefore making it distinguishable from other possible spindown processes. Furthermore, assuming one can measure the mass of the black hole, we develop a method of measuring the ultralight boson mass by means of measuring the angular diameter of the black hole shadow.

Contents

Introduction

From the first detection of gravitational waves in 2015 [1], the interest in gravitational wave sources has drawn the attention of the scientific community. This new window of radiation opens up the possibility to observe and discover new physics even beyond the Standard Model. One example of this is black hole (BH) superradiance. BH superradiance is a dissipative effect triggered by the scattering of monochromatic waves with frequency ω off rotating BHs satisfying:

$$\omega < m\Omega_H \ , \tag{1}$$

where Ω_H is the angular velocity of the event horizon and m the magnetic quantum number of the wave. As a consequence the BH loses energy and angular momentum while the wave is amplified [1]. Since the existence of an event horizon in a stationary and axisymmetric spacetime automatically implies the existence of an ergoregion [2], the Kerr metric provides a good background to study superradiance.

The first realisation of such phenomena was first studied by Teukolski and Press [3], where they proposed the "Black hole bomb", an unstable system where a spherical mirror surrounding the BH is reflecting back an electromagnetic field that gets amplified every time, resulting in an "explosion" due to the electromagnetic pressure. Later, Zouros and Eardley studied the case of massive particles strongly coupled to the BH [4], where the mass of the particle serves as a natural mirror and therefore triggers an instability. The small coupling was studied by Detweiler [5], who solved the Klein-Gordon equation and gave an analytical expression of the imaginary part of the frequency, the so called "Detweiler's approximation".

For the superradiance instability to be significant enough to manifest in an astrophysical system, the Compton wavelength of a field has to be comparable to the size of the BH. This is realized for ultralight bosons with small but non zero rest mass. In particular, for masses in the range $10^{-9} - 10^{-21}$eV, astrophysical BHs can become sensitive detectors, serving as tests for fundamental physics theories [6]. One of these particles is the QCD axion with a rest mass (in the QCD frame) of $\mu \leq 6 \cdot 10^{-10}$eV or axion-like particles that are also interesting dark matter candidates. [7].

The superradiance through the axion yields the *Axionic BH Atom* [6] (also called *Gravitational atom* for general bosonic particles or, as we prefer, *Gravatom*), a coupled system consisting of a cloud made of particles bounded to the BH, where the bounded system acts as an hydrogen atom and gravitons would be emitted by transitions between energy levels. The gravitational waves emitted by this phenomena can be detected with Advanced LIGO [8], and therefore we can constrain the mass of the ultralight boson. In this work we will treat general ultralight bosons and eventually discuss the case of the axion, which is a (pseudo)Nambu-Goldston boson.

Recently, the Gravatom has also been studied in a binary system with a BH as a companion [9], where it has been shown that, analogously to atomic physics, there can exist Rabi resonances (due to level mixings induced by the gravitational interaction with the companion) which gravitational wave signals can be feasibly detected by LISA.

[1] Superradiance is similar to the Penrose process, where an incoming particle decays within the ergoregion producing an ingoing negative-energy particle (as perceived by an observer at infinity) and an outgoing particle with more energy than the incoming one.

This year the first image of a black hole in radiofrequency was released by the Event Horizon Telescope [10], showing the possibility to measure the shadow of the black hole, i.e. the area at which photons either fall into the black hole or reach the observer. This new instrumentation allow us to measure with an angular resolution up to the order of micro-arcseconds, therefore making possible to explore electromagnetic radiation in regions of the order of the gravitational radius for supermassive black holes. Altough far from arbitrary good angular resolution, a lot of work is being done towards the improvement of the instrumentation [11]. In this study we develop a method for studying BH superradiance using gravitational lensing, in particular looking at the shadow of the black hole. The structure is as follows: in the first chapter we will derive Detweiler's approximation, solving the Klein-Gordon equation and applying an asymptotic matching expansion. Later, in the second chapter, we will explore the dynamics of the cloud around the BH and, by means of studying the different time-scales, we will constuct a physical picture of the system. Next, we will introduce gravitational lensing and focus in the Kerr BH, discussing the possibility of using gravitational lensing in order to compute the mass of the boson by observational signatures of the cloud. Finally we discuss the conclusions and open problems regarding the Gravatom.

Chapter 1

Detweiler's approximation

In order to study the interaction of an ultralight boson with a Kerr BH we will solve the Klein-Gordon equation in a Kerr metric background. We make emphasis that, for now, we are not extrictly considering an axionic particle. QCD axions, for example, are pseudo-Goldstone bosons, so they have quartic terms in the lagrangian that account for self-interactions, which will be important in discussing the dynamics of the cloud (see 2.4). Once we manipulate the Klein-Gordon equation in a suitable form, we can read an effective potential which can account for a good part of the physical phenomena. We will discuss this potential and obtain the maximum and minimum value of the Schwarzchild case. Finally we will solve the differential equations at large and small distances and match the solutions, giving an expression for the imaginary part of the frequency, which we will use in order to discuss the time-scales associated to the process.

1.1 Differential equation

We begin by solving the Klein-Gordon equation:

$$(\Box - \mu^2)\phi = 0, \tag{1.1}$$

where $\mu = \mathcal{M}G/\hbar c$ for a particle of mass $\mathcal{M}$. The metric in Boyer-Lindquist coordinates (t, r, θ, ϕ) is

$$\begin{aligned} \mathrm{d}s^2 = &-\left(1 - \frac{2Mr}{\Sigma}\right)\mathrm{d}t^2 - \frac{4Mar\sin^2\theta}{\Sigma}\mathrm{d}t\mathrm{d}\varphi + \frac{\Sigma}{\Delta}\mathrm{d}r^2 \\ &+ \Sigma\mathrm{d}\theta^2 + \left(r^2 + a^2 + \frac{2Ma^2r\sin^2\theta}{\Sigma}\right)\sin^2\theta\mathrm{d}\varphi^2, \end{aligned} \tag{1.2}$$

where

$$\Delta = r^2 + a^2 - 2Mr \quad , \quad \Sigma = r^2 + a^2\cos^2\theta. \tag{1.3}$$

M is the mass and $J = aM$ is the angular momentum of the BH. One of the properties of the Kerr BH is the existence of an ergoregion. The ergoregion is the location at which an observer is forced to co-rotate with the BH and is defined as the region between the ergosphere $r_{ergo} = M + \sqrt{M^2 - a^2\cos^2\theta}$, an infinite redshift surface, and the event horizon $r_+ = M + \sqrt{M^2 - a^2}$. In order to solve the differential equation, that is separable in the chosen Boyer-Lindquist coordinates, we use the Laplace-Beltrami operator and take the ansatz [12]

$$\phi = e^{-i\omega t}e^{im\varphi}R(r)\Theta(\theta), \tag{1.4}$$

which accounts for a stationary solution (i.e. that the system remains in the same state as the time change). We separate eq. (1.1) into

$$\frac{1}{\sin\theta}\partial_\theta(\sin\theta\partial_\theta)\Theta(\theta) + \left(\lambda - a^2\kappa^2\cos^2\theta - \frac{m^2}{\sin^2\theta}\right)\Theta(\theta) = 0, \tag{1.5}$$

$$\Delta\partial_r(\Delta\partial_r)R(r) + \left[\omega^2(r^2+a^2)^2 + a^2m^2 - 4Mar\omega m - \Delta\left(\lambda + a^2\omega^2 + \mu^2r^2\right)\right]R(r) = 0 \quad (1.6)$$

where $\kappa^2 \equiv \mu^2 - \omega^2$. Using $\Theta(\theta) = y(x)$ and $x = \cos\theta$, Eq. (1.5) becomes

$$\frac{\mathrm{d}}{\mathrm{d}x}[(1-x^2)\frac{\mathrm{d}}{\mathrm{d}x}y(x)] + \left(\lambda - a^2\kappa^2x^2 - \frac{m^2}{1-x^2}\right)y(x) = 0. \quad (1.7)$$

We see that it is the differential equation for the spheroidal wave equation (see appendix A.1)

$$\frac{\mathrm{d}}{\mathrm{d}\eta}[(1-\eta^2)\frac{\mathrm{d}}{\mathrm{d}\eta}S_{ml}(-ic,\eta)] + \left(\lambda_{ml} + c^2\eta^2 - \frac{m^2}{1-\eta^2}\right)S_{ml}(-ic,\eta) = 0,$$

with the identification $\eta = x$ and $c^2 = -a^2\kappa^2$. Thus, the eigenfunction is $y(x) = S_{ml}(-ic, \cos\theta)$. Note that for c=0 the eigenfunctions are the Legendre polynomials. Meixner- Schäfke normalization [13] yields the shperoidal harmonics

$$Z_{lm}(\theta,\varphi) = \left[\frac{2l+1}{4\pi}\frac{(l-m)!}{(l+m)!}\right]^{1/2}S_{lm}(-ic,\cos\theta)e^{im\varphi}, \quad (1.8)$$

that satisfies $\int_\Omega Z^*_{lm}Z_{l'm'}\mathrm{d}(\cos\theta)\mathrm{d}\varphi = \delta_{ll'}\delta_{mm'}$. To write Eq. (1.6) in a Schrödinger-like form, we perform the following coordinate transformation

$$\frac{\mathrm{d}r_*}{\mathrm{d}r} = \frac{r^2+a^2}{\Delta},$$

and substitute $X(r) = \sqrt{r^2+a^2}R(r)$. We then obtain

$$\left[\frac{\mathrm{d}^2}{\mathrm{d}r_*^2} + \left(\omega^2 - V\right)\right]X(r) = 0,$$

with the effective potential

$$V = -\frac{a^2m^2}{(r^2+a^2)^2} + \frac{4Mar\omega m}{(r^2+a^2)^2} + \Delta\left[\frac{\lambda + a^2\omega^2 + \mu^2r^2}{(r^2+a^2)^2} - \frac{\Delta(2r^2-a^2)}{(r^2+a^2)^4} + \frac{2r(r-M)}{(r^2+a^2)^3}\right]. \quad (1.9)$$

In the new coordinates the limits to the event horizon and to infinity are, respectively, $\lim_{r\to\infty} r_* = \infty$ and $\lim_{r\to r_+} r_* = -\infty$. The effective potential is ploted in fig. 1.1. We see that we have a centrifugal bareer close to the ergoregion followed by a potential well. From this picture we can already see that it is possible for a particle to be trapped in a keplerian orbit around the Kerr BH if its energy is below the asymptotic value of the potential. If a particle is trapped in the potential its wavefunction will be ingoing at the horizon and outgoing at infinity, representing a bound state. In the next sections we will find the minimum and maximum values of the effective potential, so we can discuss the existence of bound states in terms of the gravitational coupling $M\mu$.

1.1.1 Extremal values of the effective potential

In order to find the minimum analytically one must find the solution of a sixth order polynomial, which is a hard task to archieve. What we can try to do is to find the minimum of the Schwarzschild case ($a = 0$). The potential reads

$$V_{\mathrm{Schw}} = (r-2M)\frac{2M + r\left[l(l+1) + r^2\mu^2\right]}{r^4}, \quad (1.10)$$

and the corresponding minimum is

$$r_{\min} = \frac{l(l+1)}{3M\mu^2} + \frac{A}{3M\mu^2} + \frac{l^2(l+1)^2 - 9\left(l^2+l-1\right)\mu^2M^2}{3M\mu^2A},$$

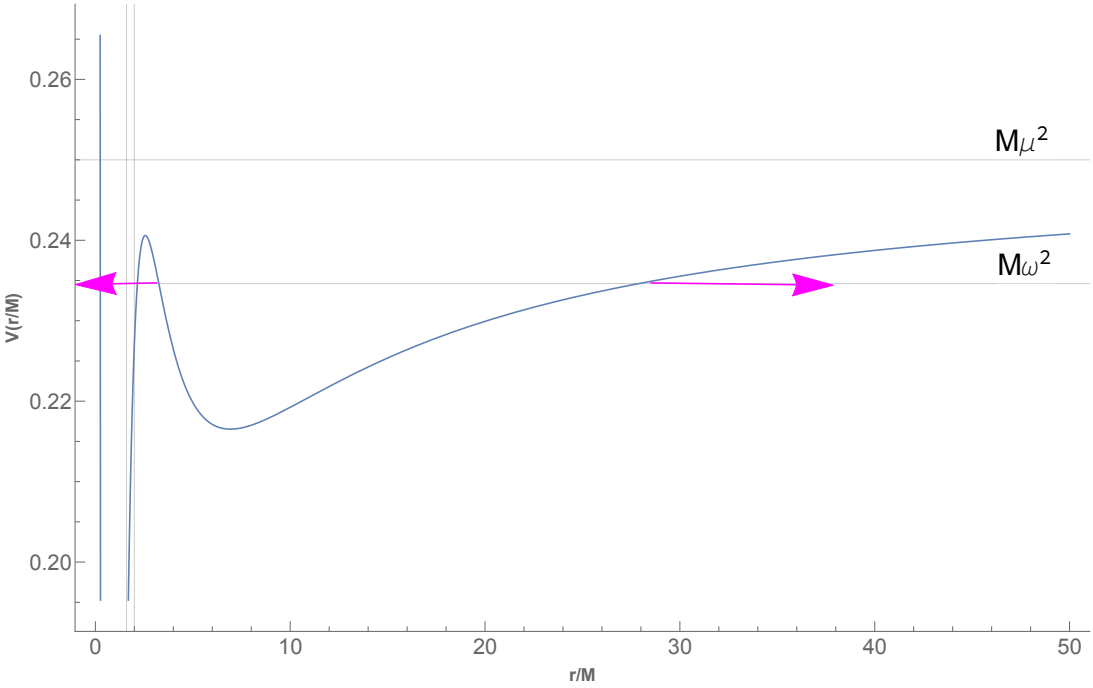

Figure 1.1: Qualitative plot of the potential (1.9) depending on r. The vertical line close to the origin is the position of the event horizon and the further vertical line corresponds to the ergoregion at $\theta = \pi/2$. The purple arrows represent the spreading of the bound state wavefunction.

with

$$A \equiv \Big\{ l^3(l+1)^3 - \frac{27}{2} l(l+1)\left(l^2+l-1\right)\mu^2 M^2 + \frac{3}{2}\Big[324\left(l^2+l-1\right)\left(l^2+l+1\right)^2\mu^6 M^6 - 3l^2(l+1)^2(l(l+1)(9l(l+1)+14)+9)\mu^4 M^4 + 5184\mu^8 M^8\Big]^{1/2} - 108\mu^4 M^4\Big\}^{1/3} .$$

If we plot this minimum and the Kerr effective potential we see that it is well approximated by the Schwarzschild case (see fig. 1.2).

The maximum correspond to the real part of one of the potential minima, explicitly

$$r_{\max} = \mathrm{Re}\left\{ \frac{l(l+1)}{3M\mu^2} - \frac{2^{2/3}\left(1+i\sqrt{3}\right)A}{6M\mu^2} - \frac{(1-i\sqrt{3})(l^2(1+l)^2 - 9(-1+l+l^2)M^2\mu^2)}{6M\mu^2 A} \right\}. \tag{1.11}$$

Again, we can plot the maximum of the potential for different spin values (Fig. 1.3) and see that it is a good approximation, roughly, up to spins $a/M = 0.3$.

1.1.2 Boundary conditions and limit solutions

By looking at the effective potential we see that bound states are formed if $\omega^2 \lesssim \mu^2$. These bound states are trapped in the potential well so that part of the wavefunction will be outgoing to infinity and part of it will be ingoing to the event horizon (see fig. 1.1).

For large radii we find $X(r) \sim e^{\pm ikr_*} \sim e^{\pm ikr}$ with $k = \sqrt{\omega^2 - V(r\to\infty)} = \sqrt{\omega^2-\mu^2}$. As we want an outgoing wave the corresponding sign is (+). Thus

$$R(r) = \frac{A}{\sqrt{r^2+a^2}} e^{i\sqrt{\omega^2-\mu^2}r} , \tag{1.12}$$

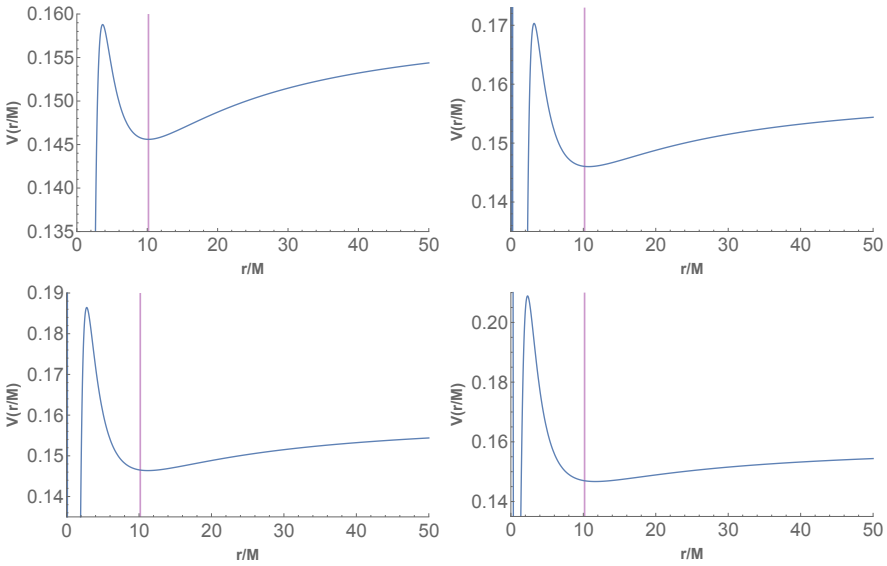

Figure 1.2: Plot of the minimum of the Schwarzschild potential (purple vertical line) for the Kerr effective potential for diferent spin parameters and a fix value of $M\mu = 0.4$ and $l = m = 1$. Top left: $a/M = 0$. Top right: $a/M = 0.3$. Bottom left: $a/M = 0.6$. Bottom right: $a/M = 0.9$

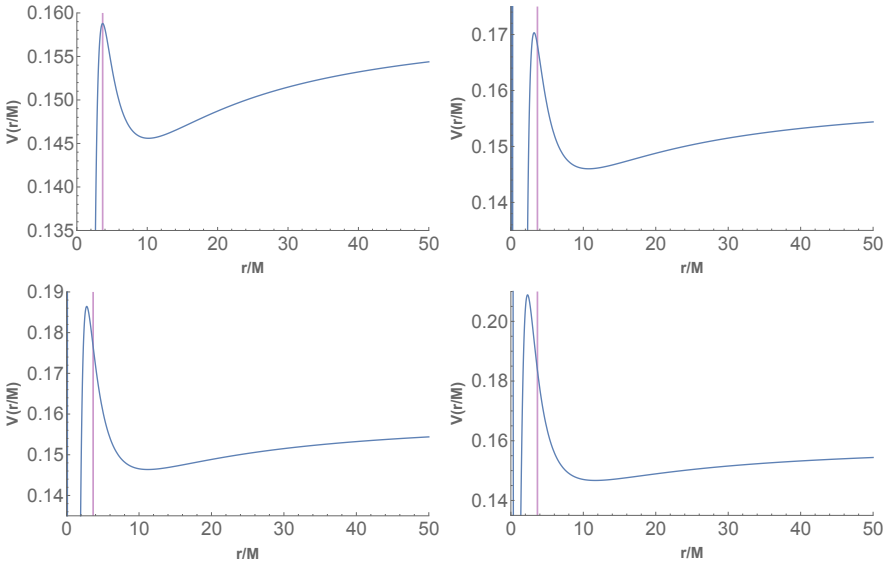

Figure 1.3: Plot of the maximum of the Schwarzschild potential (purple vertical line) for the Kerr effective potential for diferent spin parameters and a fix value of $M\mu = 0.4$ and $l = m = 1$. Top left: $a/M = 0$. Top right: $a/M = 0.3$. Bottom left: $a/M = 0.6$. Bottom right: $a/M = 0.9$

is the solution for an outgoing wave in the infinity limit.

For the event horizon limit we must discuss the boundary conditions. In the coordinate frame we may think of a solution corresponding to an ingoing wave. However, this is not correct because the wave must be ingoing for a physical observer rather than the coordinate frame. What this means is that we cannot just take $X(r) \sim e^{-ikr_*}$ but we must take into account the frame dragging effect of the Kerr black hole. Let us take an observer near the horizon. As a consequence the observer moves whitin the ergosphere with an angular velocity $\frac{\mathrm{d}\varphi}{\mathrm{d}t} = \Omega_H = \frac{a}{2Mr_+}$ (see appendix A.2). The wave solution for the observer takes the form $\phi \propto e^{-i(\omega - m\Omega_H)t} e^{\pm ikr_*}$. Taking into account $k = \sqrt{\omega^2 - V(r \to r_+)} = \omega - m\Omega_H$. The observer must see an ingoing wave and therefore we must choose the sign of k opposite to the sign of $(\omega - m\Omega_H)$:

$$m < 0: \quad \phi \propto e^{-i(\omega + |m|\Omega_H)t} e^{ikr_*} = e^{-i(\omega+|m|\Omega_H)t} e^{i(\omega+|m|\Omega_H)r_*} \qquad (\forall\omega) \tag{1.13a}$$

$$m > 0: \quad \phi \propto e^{-i(\omega - |m|\Omega_H)t} e^{ikr_*} = e^{-i(\omega-|m|\Omega_H)t} e^{i(\omega-|m|\Omega_H)r_*} \qquad (\forall\omega > m\Omega_H) \tag{1.13b}$$

$$\phi \propto e^{-i(\omega - |m|\Omega_H)t} e^{-ikr_*} = e^{i|\omega - m\Omega_H|t} e^{-i|\omega - m\Omega_H|r_*} \qquad (\forall\omega | 0 < \omega < m\Omega_H). \tag{1.13c}$$

Hence,

$$R(r) = \frac{B}{\sqrt{r^2 + a^2}} e^{-i(\omega - m\Omega_H)r_*} \ . \tag{1.14}$$

1.2 Matching solutions

In the limit of small frequencies, i.e., when the Compton wavelength of the field is much larger than the size of the BH, we can perform a matched asymptotic expansion. We divide the problem in three regions: the far, near and overlapping-region. We take the limits $r - r_+ \gg M$ and $r - r_+ \ll 1/\omega$ for the far and the near-region, respectively. Then we match the solution of both regions in the limit where $M \ll r - r_+ \ll 1/\omega$. Additionally one has the bound state condition $\omega^2 \lesssim \mu^2$ and the small mass coupling $M\mu \ll 1$. The region in which our approximations are valid is depicted in fig. 1.4.

Figure 1.4: Region in which the approximations are valid. This is: $M \ll r - r_+ \ll 1/\omega$, $M \ll 1/\mu$ and $\omega^2 \lesssim \mu^2$.

In this limit the separation constant λ of eqs. (1.5) and (1.6) behaves as [14]

$$\lambda = l(l+1) + O(a^2\omega^2), \tag{1.15}$$

which, for $M\omega \ll 1$,

$$\lambda = l(l+1) + O(a^2\omega^2) \leq l(l+1) + O(M^2\omega^2) \simeq l(l+1). \tag{1.16}$$

Therefore the spheroidal harmonics (1.8) reduce to spherical harmonics

$$Y_{lm}(\theta, \varphi) = \Big[\frac{2l+1}{4\pi}\frac{(l-m)!}{(l+m)!}\Big]^{1/2} P_{lm}(\cos\theta) e^{im\varphi}. \tag{1.17}$$

1.2.1 Far region solution

In addition to the general approximation, $M\mu \ll 1$, the far limit approximation corresponds to $r \gg r_+ + M$. Within this limit we only keep the dominant terms of (1.6) (see appendix B). This yields

$$\frac{\mathrm{d}^2}{\mathrm{d}r^2}[rR(r)] + \Big[\frac{2M\mu^2}{r} - \kappa^2 - \frac{l(l+1)}{r^2}\Big] rR(r) = 0. \tag{1.18}$$

By doing the following substitutions [5]

$$\nu \equiv M\mu^2/\kappa, \qquad \chi \equiv 2\kappa r, \tag{1.19}$$

we arrive to the Whittaker equation [13]

$$\frac{\mathrm{d}^2}{\mathrm{d}\chi^2}[\chi R(r)] + \Big[-\frac{1}{4} + \frac{\nu}{\chi} - \frac{l(l+1)}{\chi^2}\Big] \chi R(r) = 0. \tag{1.20}$$

The solution of this equation is related to the confluent hypergeometric function of first kind and second kind (or Whittaker functions) (see appendix A.3). As an analogy to the hydrogen atom case, we can define the reduced radial function $P(\chi) \equiv \chi R(r)$. The general solution is

$$P(\chi) = C_1 \chi^{l+1} e^{-\chi/2} U(l+1-\nu, 2l+2, \chi) + C_2 \chi^{l+1} e^{+\chi/2} U(l+1+\nu, 2l+2, -\chi)\,,$$

where C_1 and C_2 are constants and $U(a,b,\chi)$ is the confluent hypergeometric function of the second kind. In analogy to the hydrogen atom [15] (demanding a non-divergent behavior at $r \to 0$) we set $\nu - l - 1 \equiv n$ with n a non-negative integer. This can be seen more clearly by the fact that the confluent hypergeometric function of the second kind $U(a,b,z)$ at small values of z behaves as $U(a,b,z) \propto z^{1-b}/\Gamma(a)$. Hence, in order for the wavefunction to be zero for $z \to 0$ one must impose $a = -n$ with n a non-negative integer such that $\Gamma(a) \to \infty$.

The complex frequency (due to the dumping of the wave or, in other words, because we have quasi-normal modes) $\omega = \omega_R + i\Gamma$ will have $\Gamma < 0$ or $\Gamma > 0$ for stable and unstable modes respectively. Therefore, assuming slowly growing instabilities, we treat the imaginary part of the frequency as a first-order perturbation, i.e., $\kappa = \kappa_R\Big(1 - \frac{\omega_R}{\kappa_R^2} i\Gamma\Big) + O(\Gamma^2)$ where the quantities with subindex R correspond to those with the real part of the frequency. The real part of the frequency satisfies

$$\kappa_R^2 \equiv \mu^2 - \omega_R^2 = \mu^2 \Big(\frac{\mu M}{n+l+1}\Big)^2. \tag{1.21}$$

Taking $\mu M \ll 1$, i.e. considering ultralight bosons, we find

$$\omega_R \approx \mu\Big[1 - \frac{1}{2}\Big(\frac{\mu M}{n+l+1}\Big)^2\Big] = \mu + O(\mu M)^2, \tag{1.22}$$

and the perturbation yields $\nu = \nu + \frac{\mu^2 M \omega_R}{\kappa_R^3} i\Gamma \equiv \nu + \delta\nu$. Therefore

$$i\Gamma = \frac{\delta\nu}{M}\Big(\frac{\mu M}{n+l+1}\Big)^3. \tag{1.23}$$

Hence, for slowly growing instabilities, the imaginary part of the frequency will induce a complex ν such that $\nu - l - 1 = n - \delta\nu$. Applying the boundary conditions at infinity we set $C_2 = 0$. The solution at infinity takes the form

$$R(r) = C_1 (2\kappa r)^l e^{-\kappa r} U(-n + \delta\nu, 2l+2, 2\kappa r). \tag{1.24}$$

In order to proceed to the matching, we have to expand the solution at infinity at small values of r. In order to do so, we use the Maclaurin series of the confluent hypergeometric

function of second kind and take the behavior at $2\kappa r \ll 1$. Hence we only take into account the following terms

$$U(a,b,z) \simeq \frac{\Gamma(-b+1)}{\Gamma(1+a-b)} + z^{1-b}\frac{\Gamma(b-1)}{\Gamma(a)}. \tag{1.25}$$

Therefore, the solution in the far region, in the limit of $2\kappa r \ll 1$, becomes

$$R(r) = C_1 \frac{(2\kappa)^l \Gamma(-2l-1)}{\Gamma(-2l-n+\delta\nu-1)} r^l + C_1 (2\kappa)^{-l-1} \frac{\Gamma(2l+1)}{\Gamma(-n+\delta\nu)} r^{-l-1} \ . \tag{1.26}$$

1.2.2 Near horizon solution

In the near horizon region we take the approximation $r - r_+ \ll 1/\omega$. The differential radial equation within this limit is

$$\Delta\partial_r(\Delta\partial_r)R(r) + [r_+^4(\omega - m\Omega_H)^2 - l(l+1)\Delta]R(r) = 0 \ . \tag{1.27}$$

Substituting $z = \frac{r-r_+}{r-r_-}$ we find

$$z(1-z)\partial_z^2 R(z) + (1-z)\partial_z R(z) + \varpi^2\Big(\frac{1-z}{z}\Big)R(z) - \frac{l(l+1)}{(1-z)}R(z) = 0 \ , \tag{1.28}$$

with ϖ the superradiant factor defined as

$$\varpi \equiv (\omega - m\Omega_H)\frac{r_+^2}{r_+ - r_-} \ . \tag{1.29}$$

Since every second-order ordinary differential equation with at most three regular singular points can be transformed into the hypergeometric differential equation (see appendix A.4), we can express the radial function as $R(z) = z^{i\varpi}(1-z)^{l+1}F(z)$ [16] . Then, Eq. (1.28) becomes

$$\begin{aligned} &z(1-z)\partial_z^2 F(z) - [(l+1+2i\varpi)(l+1)]F(z) \\ &+\Big[(1+2i\varpi) - [2(l+1)+2i\varpi+1]z\Big]\partial_z F(z) = 0 \, . \end{aligned} \tag{1.30}$$

As expected, this differential equation corresponds to the hypergeometric differential equation with the following parameters:

$$a = l+1+2i\varpi, \quad b = l+1, \quad c = 1+2i\varpi, \tag{1.31}$$

The most general solution near $z = 0$ (i.e. $r = r_+$) is

$$\begin{aligned} R(z) = &Az^{-i\varpi}(1-z)^{l+1}\ {}_2F_1(a+1-c, b+1-c; 2-c; z) \\ &+ Bz^{i\varpi}(1-z)^{l+1}\ {}_2F_1(a,b;c;z) \ . \end{aligned} \tag{1.32}$$

This solution represents an ingoing and outgoing wave. As discussed in Sec. 1.1 we only want an ingoing wave and therefore we set $B = 0$. Since we are looking for the behavior at large r (i.e. $z \to 1$), we must shift the equation from z to $1-z$. This can be done with Euler's hypergeometric transformations. Therefore, taking the limit $r \to \infty$ i.e. $(1-z) \to \frac{r_+-r_-}{r}$

$$R(r) = A\Gamma(1-2i\varpi)\Big[\frac{(r_+-r_-)^{-l}\Gamma(2l+1)}{\Gamma(l+1)\Gamma(l+1-2i\varpi)}r^l + \frac{(r_+-r_-)^{l+1}\Gamma(-2l-1)}{\Gamma(-l-2i\varpi)\Gamma(-l)}r^{-l-1}\Big], \tag{1.33}$$

where we have used the property ${}_2F_1(a,b;c;0) = 1$.

1.2.3 Matching

Once we have computed the far and near-region solutions we match them to obtain the solution in the overlapping region. The matching yields

$$\frac{(r_+ - r_-)^{-l}}{\Gamma(l+1-2i\varpi)}\frac{\Gamma(2l+1)}{\Gamma(l+1)}\frac{\Gamma(-2l-n+\delta\nu-1)}{\Gamma(-2l-1)} = (2\kappa)^l, \tag{1.34a}$$

$$\frac{(r_+ - r_-)^{l+1}}{\Gamma(-l-2i\varpi)}\frac{\Gamma(-2l-1)}{\Gamma(-l)}\frac{\Gamma(-n+\delta\nu)}{\Gamma(2l+1)} = (2\kappa)^{-l-1}. \tag{1.34b}$$

Dividing eq. (1.34b) by eq. (1.34a) and using the gamma function property [17] $\Gamma(z+1) = z\Gamma(z)$, the imaginary part of the frequency reads (see appendix C)

$$\Gamma_{nlm} = -2\frac{r_+}{M}(\mu - m\Omega_H)(\mu M)^{4l+5}\gamma_{nlm}, \tag{1.35}$$

where

$$\gamma_{nlm} \equiv \frac{2^{4l+2}(2l+n+1)!}{(l+n+1)^{2l+4}(n!)}\Big[\frac{l!}{(2l)!(2l+1)!}\Big]^2\prod_{k=1}^{l}\Big[k^2\Big(1-\frac{a^2}{M^2}\Big)+4r_+^2(\mu-m\Omega_H)^2\Big].$$

As expected, for $\omega_R \sim \mu > m\Omega_H$ the imaginary part decays. However, if the superradiance condition $\omega_R \sim \mu < m\Omega_H$ is satisfied, the imaginary part becomes positive and indicates an instability. As the field has an exponential dependence $\phi \propto e^{-i\omega t} = e^{-i\omega_R}e^{\Gamma t}$ the growth is exponential with a growth timescale $\tau_{sr} = 1/\Gamma_{nlm}$. The frequency is

$$\omega_{nlm} \simeq \mu\left[1-\frac{1}{2}\left(\frac{\mu M}{n+l+1}\right)^2\right] - 2i\frac{r_+}{M}(\mu - m\Omega_H)(\mu M)^{4l+5}\gamma_{nlm}. \tag{1.36}$$

As we can see, the real part of the frequency follows a hydrogen-like spectra with principal quantum number $\tilde{n} = n + l + 1$. This is the so-called Detweiler's approximation.

From eq. (1.35) we can already see that the imaginary part of the frequency, for $M\mu \ll 1$ decreases with increasing l. Since $-l \leq m \leq l$, the maximum value of Γ_{nlm} for a given $M\mu$ will be given by $m = l$, with m such that the superradiance condition is satisfied. This can be explained by the form of the potential: the centrifugal barrier increases with l, so that the fastest growing modes will be those that enter the ergoregion easily, therefore the ones passing through a lower barrier, with smaller l, and being as high as possible in the well, therefore the ones with largest projection on the black hole rotation axis $m = l$ [18]. The radial quantum number has a mild influence [6] so for consistency we will fix it to be $n = l - 1$, although the following analysis is valid for any combination of quantum numbers.

Chapter 2

Time-scales and evolution

Let us review what we have done until now: within some approximations we have solved the Klein Gordon equation of an ultralight boson (such as an axion) and computed the real and imaginary parts of the frequency for a bound state in a keplerian orbit. This result leads to two possible scenarios: the bosonic wavefunction gets exponentially supressed for $\Gamma_{nlm} < 0$ or it grows exponentially for $\Gamma_{nlm} > 0$, triggering an instability. The more interesting case is the latter, where the condition $\Gamma_{nlm} > 0$ translates in the superradiant condition (1). Within this regime we will have an extraction of energy from the black hole to the bosonic wavefunction and a filling of different energy levels following a hydrogen-like spectra, therefore forming a cloud around the BH. In this section we aim to give a summary about the dynamics of superradiance instability following [6].

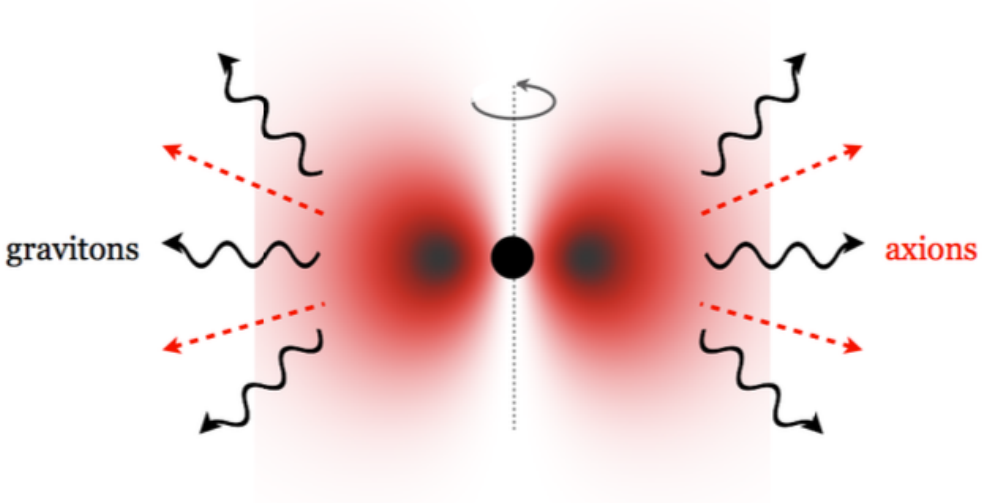

Figure 2.1: Pictorial description of the bosonic cloud around the BH. Following the analogy with the hydrogen atom, and considering axions as the ultralight bosons, instead of electrons emitting photons we have axions emitting gravitons. Picture taken from [19].

Using the Bohr approximation one can estimate the size of the cloud being

$$r_c \simeq \left(\frac{\tilde{n}}{\mu M}\right)^2 M = \left(\frac{\tilde{n}}{\alpha}\right)^2 r_g, \tag{2.1}$$

where $\tilde{n} = n+l+1$ and in the last step we have adopted the common notation in the references, being $r_g = GM/c^2$ the gravitational radius of the black hole and $\alpha = \mu r_g$ the analogous of

the atomic fine-structure constant, which in our units are equal to M and $M\mu$ respectively. Analogously one can also estimate the velocity of a particle in the level $\tilde{n}$,

$$v \simeq \frac{\alpha}{\tilde{n}} \,. \tag{2.2}$$

On the other hand, taking $\omega \sim \mu$ one can constrain the velocity by means of the superradiance condition

$$\alpha = \mu r_g \sim \omega r_g < m \frac{a}{2 r_g r_+} r_g = \frac{m}{2} \frac{a}{r_+}, \tag{2.3}$$

such that

$$v < \frac{m}{2\tilde{n}} \frac{a}{r_+} < \frac{1}{2}, \tag{2.4}$$

which means that the cloud is moderately relativistic, where the upper bound is satisfied for $a = M$ and $\tilde{n} \sim l = m \gg 1$. If we have an estimate of the velocity we can also estimate the temperature of the cloud by identifying the temperature with the average kinetic energy of a particle, which in the non-relativistic case $\alpha/l \ll 1$ is given by

$$K_B T_c = \frac{1}{2} \mu \langle v \rangle^2 .$$

For the mean velocity we will take the velocity corresponding to the dominant mode of the cloud $\tilde{l}$

$$\langle v \rangle \simeq \frac{\alpha}{\tilde{l}},$$

and therefore the temperature reads

$$T_c = \frac{\mu}{2K_B} \left(\frac{\alpha}{\tilde{l}} \right)^2 .$$

By means of eq. (2.4) we see that the temperature is bounded by

$$T_c < \frac{\mu}{8K_B} = 1.4 \times 10^{-8} K \left(\frac{\mu}{10^{-11}\text{eV}} \right).$$

Finally, we can estimate the mass of the cloud M_c as the difference between the initial and final mass of the BH after the instability [20]. In order to do the computation we will use eq. (2.7)

$$M_f - M_i = \frac{\omega}{m} (J_f - J_i),$$

which yields

$$M_c = M_i - M_f = \frac{\omega}{m} (J_i - J_f) = \frac{\omega J_i}{m} - \frac{4\omega M_f r_{g,f} \alpha_f}{m^2 + 4\alpha_f^2} \simeq \frac{\omega J_i}{m} = \frac{\omega a M_i}{m} = M_i \frac{\alpha_i}{m} \frac{a}{r_g}, \tag{2.5}$$

where for the final angular momentum of the BH we used eq. (2.3) in the saturation of the superradiance condition and we have assumed $\alpha_f \ll 1$. In fig. 2.2 we have plotted the ratio of the mass of the cloud to the mass of the black hole for $\mu = 0.7 \times 10^{-11}$eV and $a = 0.8M$ (which we treat in sec. 2.3). The case of mass $10 M_\odot$ corresponds to a mass coupling of $\alpha = 0.5$ such that our approximations are valid up to that value. We see that, for a more conservative value of M, the mass of the cloud is of order of 10% the mass of the black hole.

As a summary we have listed all the parameters in table D.1, where we show the correspondent expression and some typical values.

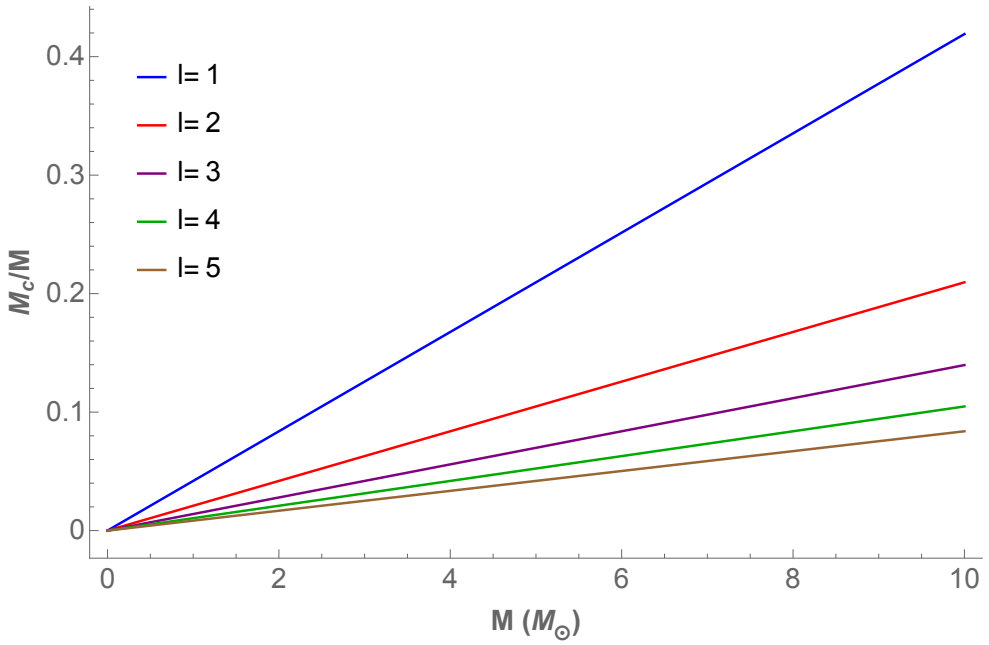

Figure 2.2: Ratio of the mass of the cloud M_c and the mass of the black hole M for $\mu = 0.7 \times 10^{-11}$eV and $a = 0.8M$ and different $l = m$ and $n = l + 1$ levels.

Cloud parameter	Expression	Typical values
Radius	$r_c = \left(\frac{\tilde{n}}{\alpha}\right)^2 r_g$	$2.5 \times 10^{37}\text{Km} \left[\tilde{n}^2 \left(\frac{10M_\odot}{M}\right) \left(\frac{10^{-12}\text{eV}}{\mu}\right)\right]$
Velocity	$v \simeq \frac{\alpha}{\tilde{n}}$	$0.07c \left[\tilde{n}^{-1} \left(\frac{M}{10M_\odot}\right) \left(\frac{\mu}{10^{-12}\text{eV}}\right)\right]$
Temperature	$T_c = \frac{\mu}{2K_B} \left(\frac{\alpha}{\tilde{l}}\right)^2$	$3 \times 10^{-11} K \left[\tilde{l}^{-2} \left(\frac{M}{10M_\odot}\right)^2 \left(\frac{\mu}{10^{-12}\text{eV}}\right)^3\right]$
Mass	$M_c = M_i \frac{\alpha_i}{m} \frac{a}{r_g}$	$0.6M_\odot \left[\left(\frac{M}{10M_\odot}\right)^2 \left(\frac{\mu}{10^{-12}\text{eV}}\right) \left(\frac{a}{0.8r_g}\right) \left(\frac{1}{l}\right)\right]$

Table 2.1: Summary of the derived parameters. Here we show the expression in Planck units and some typical values in SI units for $M = 10M_\odot$ and $\mu = 10^{-12}$eV.

2.1 Energy balance

In this section we investigate the effect of superradiance in the energy balance. In particular we will follow [21], where the energy balance is derived using Hawking's area theorem. We will see that, as said before, the superradiance condition implies an extraction of energy from the black hole that translates in a decrease in the mass and spin of the BH. The area of a Kerr BH is [22]

$$A = 4\pi(r_+^2 + a^2),$$

differentiating the area yields

$$\delta A = 16\pi \frac{r_+^2 + a^2}{r_+ - r_-}(\delta M - \Omega_H \delta J), \tag{2.6}$$

with J the BH angular momentum, $r_- = M - \sqrt{M^2 - a^2}$ and Ω_H the horizon angular velocity. For a given field we can relate its energy and angular momentum to the one of the BH. Let's consider a Kerr spacetime with Killing vectors $\xi^\mu_{(t)} \equiv \partial^\mu t$ and $\xi^\mu_{(\varphi)} \equiv \partial^\mu \phi$. Their respective conserved energy fluxes are

$$\epsilon^\mu = -T^\mu_\nu \xi^\nu_{(t)}, \qquad l^\mu = T^\mu_\nu \xi^\nu_{(\varphi)},$$

such that the energy and angular momentum flux through a hypersurface $d\Sigma_\mu$ are

$$\delta E = \epsilon^\mu d\Sigma_\mu, \qquad \delta L = l^\mu d\Sigma_\mu.$$

Taking a spherical surface $d\Sigma_\mu = n_\mu r^2 dt d\Omega$ with n_μ the (radial) outgoing normal vector to the surface, the ratio between energy and angular momentum is given by

$$\frac{\delta E}{\delta L} = -\frac{T^r_t}{T^r_\varphi}.$$

Considering a scalar field $\phi(t, r, \theta, \phi) = f(r, \theta) e^{-i\omega t} e^{im\varphi}$ with energy-momentum tensor

$$T_{\mu\nu} = \nabla_\mu \phi \nabla_\nu \phi - g_{\mu\nu} \left(\frac{1}{2} \nabla_\alpha \phi \nabla^\alpha \phi + V(\phi) \right) .$$

yields

$$\frac{\delta E}{\delta L} = -\frac{T^r_t}{T^r_\varphi} = -\frac{\nabla^r \phi(-i\omega\phi)}{\nabla^r \phi(im\phi)} = \frac{\omega}{m}. \tag{2.7}$$

Conservation of angular momentum and energy implies that a change of the angular momentum and energy of the wave, will occur at expenses of a change of angular momentum and energy of the BH: $\delta L = \delta J$ and $\delta E = \delta M$. Therefore, subtituting in eq. (2.6) we obtain

$$\delta M = \frac{\omega}{16\pi} \frac{r_+ - r_-}{r_+^2 + a^2} \frac{\delta A}{\omega - m\Omega_H}. \tag{2.8}$$

The area theorem implies that $\delta A \geq 0$ [19] and, if the superradiant condition is met, the field extracts energy from the horizon $\delta M < 0$.

2.2 Kinetic equations

In order to study the dynamics of the cloud, it is natural to look at the different time-scales of possible physical phenomena involved in the dynamical evolution of the cloud. As before, we are not assuming that the boson is an axion, although in sec. 2.4 we will discuss the axion case. We will start, first of all, looking at the kinetic equations. Later, we will discuss the possibility of gravitational wave emission and, last but not least, the possible phenomena emerging from considering the axion, where we will look at axion non-linear effects by the cloud itself.

Given that the superradiant time-scale Γ^{-1}_{nlm} is larger than the dynamical time-scale of the black hole r_g we can assume a quasi-adiabatic evolution and treat the non-linear effects as perturbations since these will become relevant when the system is still in the quasi-linear regime [6][23]. Therefore the set of kinetic equations corresponding to the occupation numbers N_i for different levels is

$$\frac{dN_i}{dt} = \Gamma_{ij} N_j + \Gamma_{ijk} N_j N_k + \dots . \tag{2.9}$$

For simplicity we have dropped N_i-independent terms corresponding to spontaneous emission. The linear regime corresponds to truncation of the set of equations up to the first term, by which we will start with.

2.2.1 Instability time-scale

For the superradiance process, the linear coefficient corresponds to the imaginary part of the frequency given by

$$\Gamma_{ij} = \delta_{ij}\Gamma_i \ , \tag{2.10}$$

where the index corresponds to some level and Γ_i is given by eq. (1.35). In order to put some numbers we need to fix either the mass of the BH or the mass of the boson. We will fix the mass of the BH to be $M = 6M_\odot$ and change the mass of the boson as well as the energy levels.

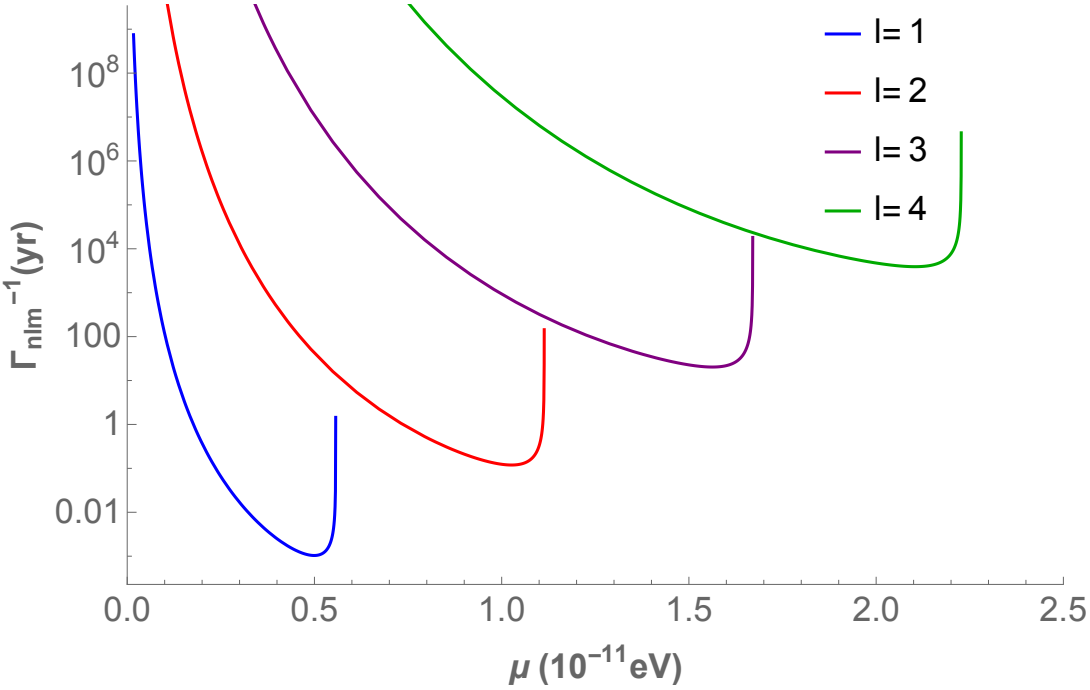

Figure 2.3: Instability time-scale. We plot the time-scale $\tau_{sr} = 1/\Gamma_{nlm}$ as a function of the mass μ of the particle for $m = l = n + 1$ and different values of l. We have chosen a BH with mass $M = 6M_\odot$ and spin $a = 0.8M$.

As we can see in fig. 2.3, in agreement of what we said in sec. 1.2 the fastest level is the one with the smallest l and $m = l$. In fig. 2.4 we see that the instability increases with the spin, so the instability time-scale will be shorter for large spins. This can be seen by looking at eq. (1.35), where for a fixed frequency ω and μ, the magnitude of the instability will increase with the angular velocity of the ergoregion, which increases with the spin of the BH. Physically this means that the faster the BH rotates, the faster the field extracts energy from it and therefore the instability time-scale is shorter.

One may wonder if it is possible to have electromagnetic emission but, as showed in [6], in the case of the axion, the axion-photon conversion is too slow to be relevant for the dynamics of superradiance.

In the next section we explore the gravitational wave emission, which correspond to non-linear terms in (2.9).

2.2.2 Cloud depletion time-scale

One can reasonably expect that, as an analogy of the hydrogen atom, the bosons will emit gravitons due to level transitions and one-graviton annihilation of two bosons (since our space-time is curved this can happen, contrary to flat spacetime, where it's forbidden by energy and momentum conservation). The latter is of special interest since the cloud can eventually

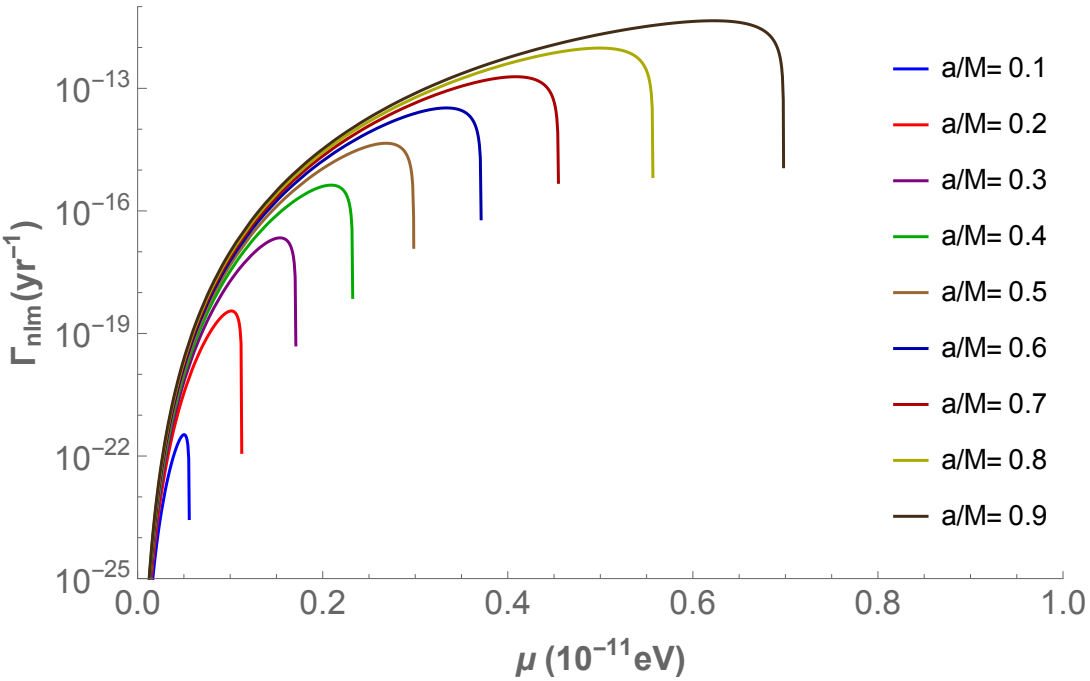

Figure 2.4: Inverse of the time-scale for different spins. We plot the imaginary part of the frequency Γ_{nlm} as a function of the mass μ of the particle for different values of a. We have chosen a BH with mass $M = 6M_\odot$ and $l = 1$, $n = l - 1 = 0$. We show the inverse value in order to have a clear plot, otherwise the logarithmic scale takes negative values.

deplete annihilating all the bosons into gravitons, which will play an important role into the evolution of the system. We will follow the same strategy as the literature ([8],[9]), this is, from the power and energy consevation we will compute the mass evolution and identify the time-scale. For the power of the gravitational wave emission via annihilation, due to the heavy computational cost, we will use the flat approximation formula of ref. [24], which is a good approximation of the numerical results for $\alpha \ll 1$ and also agree with the numerical results of ref. [20]. This formula is obtained by computing the perturbation of the metric in the Einstein field equation, in the flat metric background. For a detailed computation and discussion we refer to ref. [24]. The expression for the power reads

$$\frac{dE_{\rm gw}}{dt} = C_{nl}\left(\frac{M_c(\alpha)}{M}\right)^2 \alpha^{Q_l} \ ,$$

where $M_c(\alpha)$ is the mass of the cloud, eq. (2.5), and

$$C_{nl} = \frac{16^{l+1} l(2l-1)\Gamma(2l-1)^2\Gamma(l+n+1)^2}{n^{4l+8}(l+1)\Gamma(l+1)^4\Gamma(4l+3)\Gamma(n-l)^2} \ , \qquad Q_l = 4l + 10 \ .$$

Assuming that there is no other process that extracts mass from the BH (e.g. accretion disks), conservation of energy implies that $-\dot{M}_c = \dot{E}_{\rm gw}$. This condition yields

$$M_c(t) = \frac{M_{c,0}}{1 + t/\tau_{\rm GW}} \ ,$$

with $M_{c,0}$ the initial mass of the cloud and $\tau_{\rm GW}$ the time-scale of the process,

$$\tau_{\rm GW} = \frac{l}{C_{nl}}\left(\frac{r_g}{a}\right) M\alpha^{-(Q_l+1)} \ . \tag{2.11}$$

We will see that the depletion time-scale is orders of magnitude larger than the instability time-scale. In order to compute the annihilation rate we will use the following formula:

$$\Gamma_a \equiv \frac{\dot{E_{\rm gw}}}{2\omega} \ . \tag{2.12}$$

We divide the power by the frequency of the emitted graviton in order to get the rate of emission of a single graviton. Altough we didn't make use of the annihilation rate, we will use this result when discussing the evolution of the system (sec. 2.3), where we will se that the effect of the cloud depletion is significant only in the saturation of the superradiance condition.

2.3 System evolution

When the superradiance condition is saturated one can compute the Regge trajectories, the lines in the BH spin vs BH mass plane at which, for a given level, superradiance will stop developing. The condition is given by the equality (2.3) and yields

$$\frac{a}{r_g} = \frac{4m\alpha_f}{m^2 + 4\alpha_f^2} \ , \tag{2.13}$$

with α_f corresponding to the final BH mass. In fig 2.5 we have plotted the Regge trajectories with the additional condition of the instability to last less than the age of the Universe ($\sim 10^{10}$yr). Therefore, we can only be able to observe superradiance in black holes inside the shaded regions corresponding to different levels.

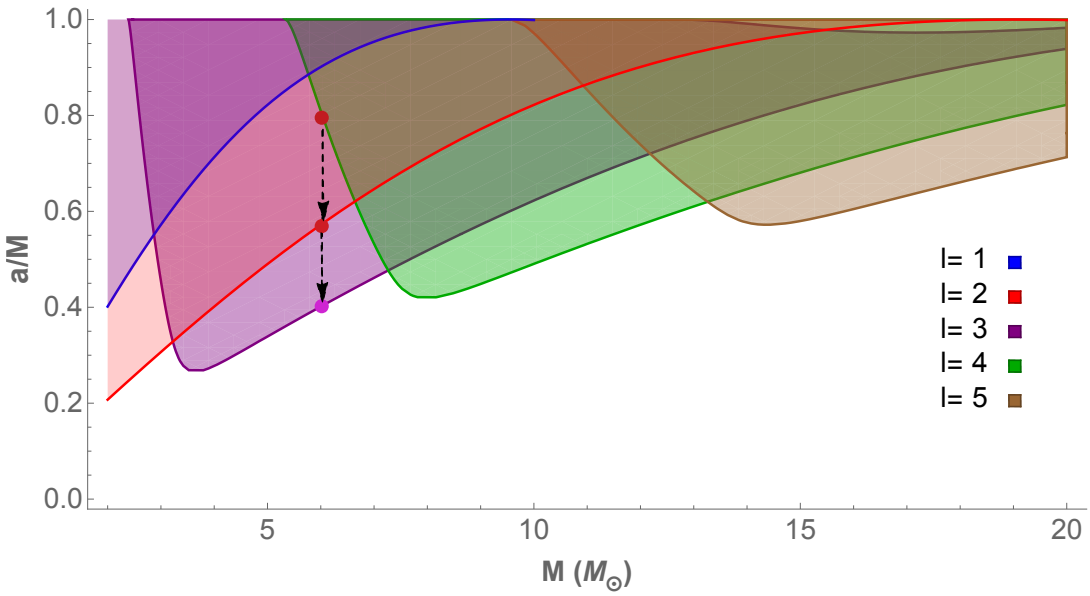

Figure 2.5: Regge trajectories. Plot of the black hole spin (a/M) vs the black hole mass M in units of solar mass. The axion mass has been set to $\mu = 0.7 \times 10^{-11}$eV. The trajectories are computed by requiring that the time-scale of the instability is less than the age of the Universe in order to discuss the observational properties.

Taking into account the phenomena described until now we can construct a qualitative picture of what it is happening within the system (see fig. 2.6). First of all, a Kerr black hole interacts with the ultralight boson (which until now can be an axion field or not) and a cloud is formed. We will consider the $l = m = n + 1 = 1$ level. Within this scenario we will have emission of gravitational waves (GWs) due to transitions between different levels. As the cloud

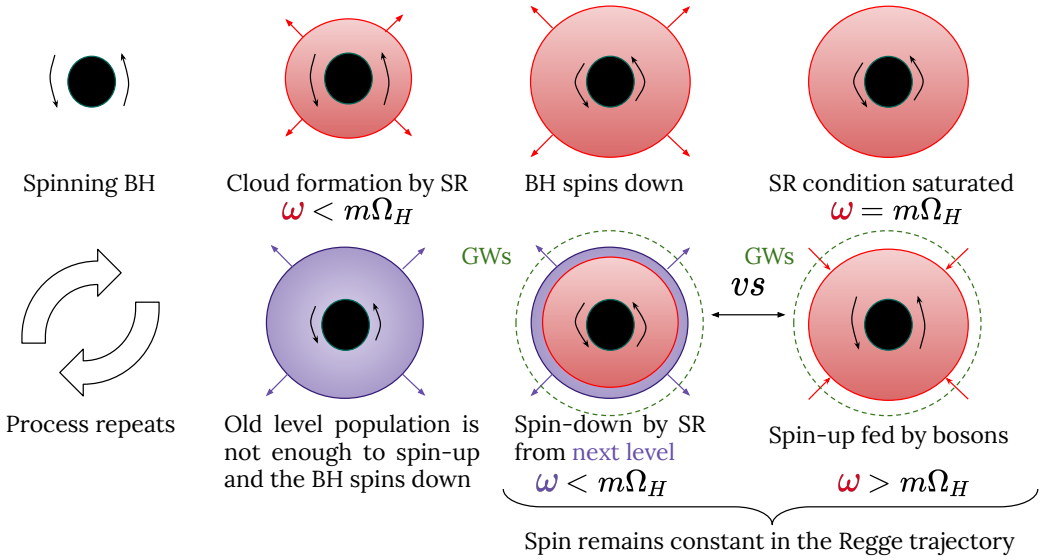

Figure 2.6: Pictorial description of the evolution of the BH-ultralight boson system. This description corresponds to neglecting axion non-linear effects.

is growing due to superradiance, it extracts mass and spin from the BH until the superradiance condition is saturated for the $l = m = 1$ level (see sec. 2.1). Once this happens, superradiance will stop for the $l = m = 1$ level and the $l = m = 2$ level will start growing. Looking at the kinetic equations we see that the cloud depletion by GWs will be less important in the beggining of the superradiant process and will be significant when the superradiance condition is saturated. Indeed, the kinetic equation reads

$$\frac{dN}{dt} = \Gamma_{nlm} N - \Gamma_a N^2,$$

with

$$\Gamma_{nlm} = -\frac{r_+}{r_g}(\mu - m\Omega_H)\alpha^{4l+5}\gamma_{nlm}, \tag{2.14}$$

$$\Gamma_a = \frac{\dot{E}_{\rm gw}}{2\omega} = \frac{r_g}{2l^2} C_{nl} \alpha^{4l+11} \left(\frac{a}{r_g}\right)^2. \tag{2.15}$$

Hence, for $\alpha \ll 1$ the cloud depletion is not significant for the evolution of the system until $\Gamma_{nlm} = 0$ with the saturation of the superradiance condition. Therefore, after superradiance saturation, the remaining cloud will start emitting GWs due to one graviton annihilation of two bosons and will also start feeding the BH, which results in a spin-up of the system. The feeding of the BH by bosons happens atfer the saturation of the superradiance condition, i.e. $\omega_{l=m=1} > \Omega_H$ (see eq. (2.8)). At this point we have a competition between the spin-up due to the $l = m = 1$ level and the spin-down due to the $l = m = 2$ level. Using the kinetic equations this translates into the condition

$$\left|\frac{dN_{l=m=1}}{dt}\right| = \left|\frac{dN_{l=m=2}}{dt}\right|,$$

which gives $N_{l=m=1} = \left|\frac{\Gamma_{322}}{\Gamma_{211}}\right| N_{l=m=2}$. In this stage the BH remains in the Regge trajectory $a_{l=1}/r_g$ for a long time until the $l = m = 1$ level gets depopulated. Now when $N_{l=m=1} < \left|\frac{\Gamma_{322}}{\Gamma_{211}}\right| N_{l=m=2}$ the spin-down due to the $l = m = 2$ level wins and the process starts again until

reaching the next Regge trajectory $a_{l=2}/r_g$, where it will keep going until the superradiance rate is too slow to be possible. In order to put some sumbers, similar to [8], let's consider a $6M_\odot$ BH with spin $a = 0.8M$ and a boson field of $\mu = 0.7 \times 10^{-11}$eV. With these parameters the BH will start populating the $l = m = 2$ level (upper red dot of fig. 2.5). This process wil take the order of one and a half years, where the BH will spin down to $a = 0.57M$ and remain in the red line (second red dot) for 10^5yr (eq. (2.11)). After the $l = m = 2$ cloud dissipates, superradiance will start populating the $l = m = 3$ level, which will take of the order of 8×10^4yr until reaching the purple line (purple dot), with a spin $a = 0.40M$, where it will remain for 10^{11}yr.

2.4 Axion non-linearities

Another source of non-linear terms in (2.9) is the axion self-interaction. Since the axion is a (pseudo)Nambu-Goldstone boson, the axion Lagrangian must contain the quartic self-interaction term

$$\mathcal{L} = -\frac{1}{2} g^{\mu\nu} \nabla_\mu \phi \nabla_\nu \phi - \frac{1}{2}\mu^2\phi^2 + \frac{1}{16}\left(\frac{\mu}{f_a}\right)^2 \phi^4 \ , \tag{2.16}$$

where f_a is the decay constant, the scale of spontaneous symmetry breaking. In the non-relativistic limit the axion field can be expressed as

$$\phi = \frac{1}{\sqrt{2\mu}}(e^{-i\mu t}\psi + e^{i\mu t}\psi^*) \ , \tag{2.17}$$

where the field ψ varies in a timescale larger that μ^{-1}. If one computes the action and drops all rapidly oscillating terms, one obtains an effective, non-relativistic action

$$S_{nr} = \int \mathrm{d}x^4 \sqrt{-g}\left[-\frac{1}{2\mu}\nabla_\alpha\psi^*\nabla^\alpha\psi - \frac{i}{2}g^{0\alpha}\left(\psi^*\nabla_\alpha\psi - \psi\nabla_\alpha\psi^*\right) - \mu\left(\frac{g^{00}+1}{2}\right)\psi^*\psi + \frac{1}{16 f_a^2}\left(\psi^*\psi\right)^2\right], \tag{2.18}$$

which describes an interacting Bose-Einstein Condensate (BEC), since it leads to the non-linear Gross-Pitaevskii equation. If the atractive force between bosons gets stronger as the number of bosons increase, there will be a competition between potential and self-interaction energy of the cloud [6]

$$\frac{\alpha}{r} \sim \frac{\psi^*\psi}{8 f_a^2} \ .$$

Integrating both sides over the volume and taking into account that $N = \int d^3x \ \psi^*\psi$, we can obtain the threshold as a function of the number of bosons

$$N \geq 16\pi\alpha f_a^2 r_c^2 \sim 16\pi f_a^2 r_g^2 \left(\frac{l^4}{\alpha^3}\right) \ ,$$

and relate it to the mass of the cloud $M_c = N\mu$,

$$\frac{M_c}{M} \geq 2\frac{l^4}{\alpha^2}\frac{f_a^2}{M_{Pl}^2} \ . \tag{2.19}$$

Above this mass the self-interaction energy becomes more important than the potential energy and the form of the cloud cannot be described by the hydrogenic solutions. If the self-interaction energy grows enough, the cloud will colapse in what is called a Bosenova, an effect associated to the BEC. If a Bosenova occurs, part of the cloud falls into the BH and the rest escapes to infinity emitting a gravitational wave burst [8]. This will spin-up the BH and start superradiance again, therefore entering into a cycle of Bosenova explosions until enough energy is radiated away such that superradiance cannot happen again.

In order to study the effects of the self-interactions in the level-mixing, i.e. having more than one level populated at the same time, one can use the Bogoliubov approximation and express the wavefunction as $\psi = \psi_0 + \delta\psi$ where ψ_0 is the field in the most populated level and $\delta\psi$ is a perturbation in the field occupying a different level [6]. Solving the equation for the perturbation, obtained by the action, yields

$$\delta\psi = e^{-i(\omega_0 t - m_0\varphi)}\left(u(r,\theta)e^{-i(\delta\omega t - \delta m\varphi)} - v^*(r,\theta)e^{i(\delta\omega t - \delta m\varphi)}\right),$$

which is a mix between positive and negative frequencies (Bogoliubov quasiparticles). This mix of frequencies can either favor or disfavor the superradiant process since each frequency can be in different energy levels. We refer to ref. [6] for a discusion and derivation of the results. In there, after computing the energy flux at the horizon and using the results of the WKB approximation for $\alpha \gg 1$, they relate the perturbation terms to the Gross-Pitaevskii equation and find that, for the perturbation to be superradiant, the mass of the cloud must follow

$$\frac{M_c}{M} \leq \left|\frac{\Gamma_{l+1}}{\Gamma_{l-1}}\right|^{1/2} 2\frac{l^4}{\alpha^2}\frac{f_a}{M_{Pl}^2}\ , \tag{2.20}$$

or, in terms of the number of axions,

$$N \leq \left|\frac{\Gamma_{l+1}}{\Gamma_{l-1}}\right|^{1/2} 16\pi\alpha {f_a}^2 r_c^2\ ,$$

where Γ_{l+1} and Γ_{l-1} are the instability rates (computed in the Detweiler approximation) of the level above and below the most populated one. This introduces extra factors to take into account in the evolution of the cloud. In particular, going back to the example discussed above, when the $l = m = 2$ level gets saturated, superradiance for $l = m = 3$ will not occur until inequality (2.20) is satified. We see that if a superradiant level is populated enough, the number of particles can be larger than the right hand side and hence superradiance can be supressed.

Chapter 3

Gravitational lensing by a Kerr black hole

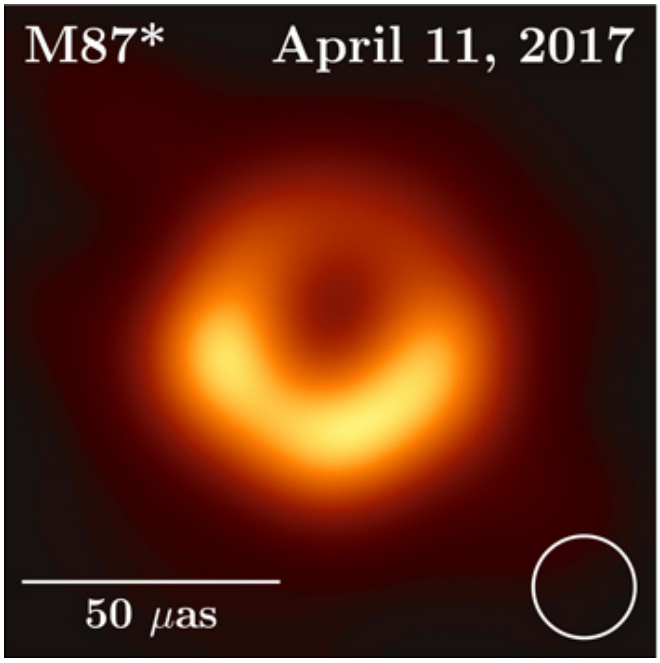

Figure 3.1: First image of a BH in the radiofrequency spectrum done by the Event Horizon Telescope. The BH mass is estimated to be $6.2^{+1.1}_{-0.6} \times 10^9 M_\odot$ and is located at 16.8 ± 0.8Mpc. Image taken from [10].

Although far from the needed resolution, a lot of advance in observing a black hole has been done. One of the most recent examples is the first image of a black hole in the radiofrequency band by the Event Horizon Telescope [10] (fig. 3.1). The following chapters aim to answer the following question: can we observe, i.e., measure the effect of such a BH-cloud system? In order to find a proper answer we will start with a review of gravitational lensing, then study a spherically symmetric BH (e.g. Schwarzschild BH) and finally the Kerr BH. In the next chapter we will modelize and discuss the effect of the bosonic cloud and finally the observational properties of such system.

3.1 Introduction to gravitational lensing

Gravitational lensing is the phenomena by which light gets deflected by the gravitational influence of a massive body. It was one of the first experimental tests of the theory of General Relativity. This effect is due to the spacetime curvature near a planet, a star or whatever cluster of matter (e.g. galaxy clusters). For the introduction we will follow ref. [25] and for the black hole lensing we will mainly follow ref. [26] and [27].

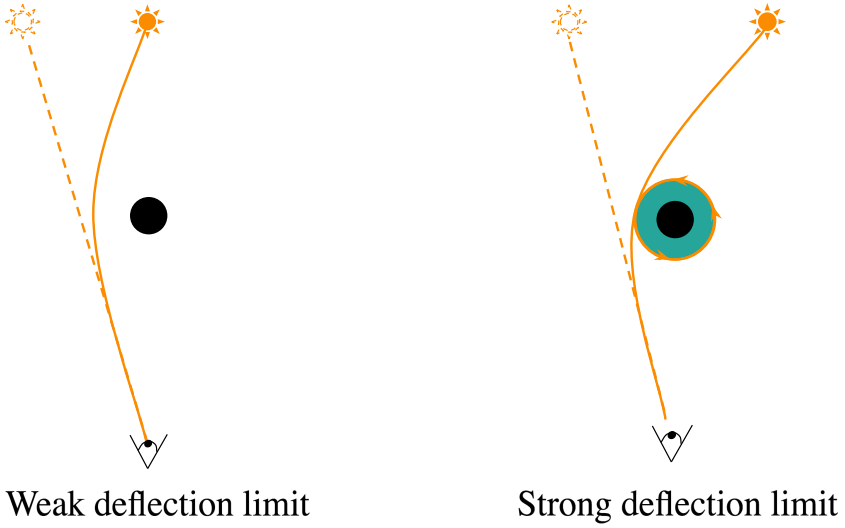

Figure 3.2: Weak deflection limit and strong deflection limit. In the strong deflection limit the green circle corresponds to the photon sphere, the region at which photons execute unstable circular orbits and can either fall into the black hole or scape to infinity and reach the observer.

The strategy for studying gravitational lensing consists of computing the geodesics of photons reaching the observer taking into account different parameters such as the observer orientation, the impact parameter or the spin of the black hole. In general the equations are solved in two limits, namely the weak deflection limit (WDL) and the strong deflection limit (SDL) (see fig. 3.2). The weak deflection limit is the assumption that the distance of closest approach r_m of the photon is larger than the gravitational radius, i.e. $r_m \gg r_g$. It is called the weak deflection limit because the deflection of the photon geodesic decreases with the distance of closest approach (see eq. (3.4)). On the other hand, the strong deflection limit takes into account that the distance of closest approach is close to the gravitational radius, where the deflection is important and the photon can perform loops around the black hole in unstable circular orbits.

3.2 Spherically symmetric black hole

Consider a general static spherically symmetric spacetime

$$ds^2 = -A(r)dt^2 + B(r)dr^2 + C(r)d\Omega^2, \quad d\Omega^2 \equiv d\theta^2 + \sin^2\theta d\varphi^2 \ . \tag{3.1}$$

In order to study the deviation of a particle (which can be a photon) by a (spherically symmetric) star, e.g. the Sun, we will consider the plane $\theta = \pi/2$ and by means of constants of motion we will derive the integrals of motion. For this spacetime the conserved quantities

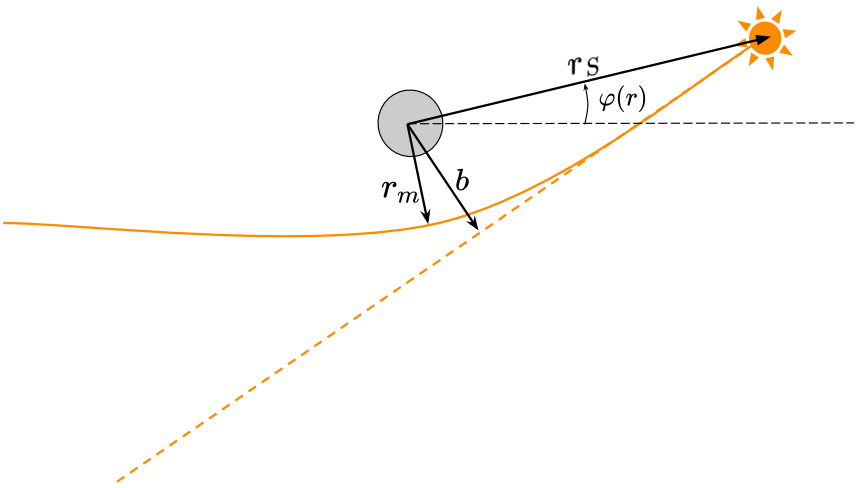

Figure 3.3: Parameters related to the deflection of light.

read (we will see this in detail for the Kerr black hole)

$$L = C(r)\frac{d\varphi}{d\lambda} \ , \qquad E = -A(r)\frac{dt}{d\lambda} \ .$$

Furthermore we can use that $g_{\mu\nu}u^\mu u^\nu \equiv \kappa$ with $\kappa = 0$ for massless particles and $\kappa = -1$ for massive particles. After some manipulation we get

$$\left(\frac{d\varphi}{dr}\right)^2 = \frac{B(r)}{C(r)^2\left(\frac{\kappa}{L^2} - \frac{1}{C(r)} + \frac{E^2}{L^2A(r)^2}\right)} \ . \tag{3.2}$$

On the other hand we can also get the following equation corresponding to a Newtonian effective potential (second and third term)

$$\frac{1}{2}\left(\frac{dr}{d\lambda}\right)^2 + \frac{L^2}{2C(r)B(r)} - \frac{E^2}{2A(r)B(r)} - \frac{\kappa}{2} = 0,$$

which considering a photon in a circular orbit in the point of closest approach $r = r_m$, i.e. $dr/d\lambda|_{r=r_m} = 0$ yields

$$\frac{E^2}{L^2} = \frac{A(r_m)}{C(r_m)} \ .$$

Inserting this in equation (3.2) we obtain

$$\varphi = \int b\sqrt{\frac{B(r)}{C(r)\left[\frac{\kappa}{b^2L^2} + \frac{C(r)}{A(r)} - b^2\right]}}dr \ , \tag{3.3}$$

with $b^2 = L^2/E^2 = C(r_m)/A(r_m)$ being the impact parameter. The impact parameter is defined as the closest distance to the origin that the particle would reach if moving in a straight line determined by its initial velocity v far from the origin [28]. If we compute the angular momentum of a photon of linear momentum p approaching the black hole from far away

$$L = rp\sin\theta = bp \ ,$$

and considering that for a photon $p = E$ we see that indeed we obtain $b = L/E$. Defining the light coming from infinity to be at $\varphi = 0$ we can express the deviation of light from going into a straight line as $\Delta\varphi = \varphi - \pi$. Einstein solved this integral assuming that $r \geq r_m \gg 2M$ (in the weak deflection limit) yielding the *Einstein angle*,

$$\Delta\varphi = \frac{4M}{b} \ , \tag{3.4}$$

with $b \simeq r_m$.

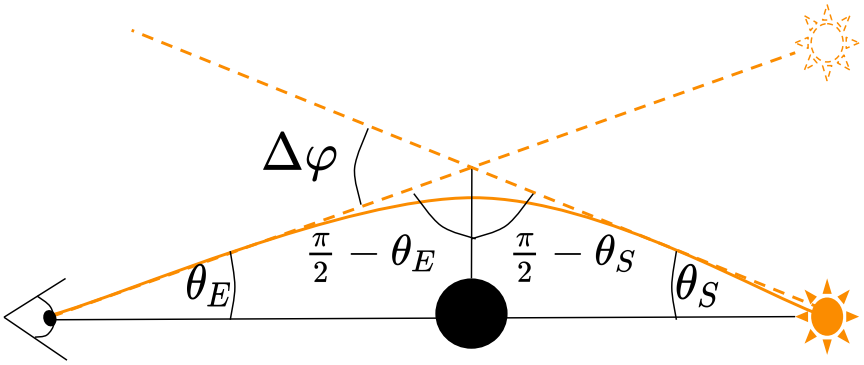

Figure 3.4: Geometry of the system. The observer's sky plane is perpendicular to the line joining the observer and the black hole.

We can also relate the Einstein angle to the angle at which an observer in the Earth will detect the photons coming from a source behind the black hole. Looking at fig. 3.4 we see that

$$\pi - (\frac{\pi}{2} - \theta_E) - (\frac{\pi}{2} - \theta_S) = \theta_E + \theta_S = \frac{4M}{b} \ .$$

Taking into account that

$$\tan\theta_S = \frac{b}{r_S} \ , \qquad \tan\theta_E = \frac{b}{r_o} \ ,$$

and using the small angle approximation $\tan\theta \simeq \theta$ yields the *Einstein ring*

$$\theta_E = \sqrt{\frac{4Mr_S}{r_o(r_o + r_S)}} \ . \tag{3.5}$$

This is the angular distance at which an observer detects the photons coming from the source, where they will form a ring of light around the black hole. This is due to the rotational symmetry around the observer-BH line. We also have Einstein rings for a Kerr black hole when the observer is situated in the pole.

3.3 Kerr black hole

Kerr black holes are not spherically symmetric (but axisymmetric), so the treatment of geodesics is not as easy as the Schwarzchild case. It makes useful to use the Hamilton-Jacobi formalism

for the geodesics since this treatment permits to write down our physical quantities in terms of integrals of motion. In order to derive the corresponding integrals of motion we will use two concepts: the conserved quantities and geodesic equation. A conserved quantity is defined as a physical parameter (or a combination of them) conserved along a geodesic, which corresponds to a symmetry of the system. In general relativity a conserved quantity $\mathcal{G}$ along a geodesic is given by a Killing vector k_μ associated to such a symmetry

$$\mathcal{G} = k_\mu u^\mu, \qquad u^\mu = \frac{dx^\mu}{d\lambda} \equiv \dot{x}^\mu,$$

where u^μ is the four-velocity along a geodesic parametrized by the affine parameter λ. For the Kerr spacetime we have two Killing vectors, $k^\mu = (1,0,0,0)$ and $m^\mu = (0,0,0,1)$, coming from the fact that the metric does not deppend explicitly on t and φ. Therefore the two conserved quantities are

$$\begin{aligned} E \equiv& - k_\mu u^\mu = -g_{t\mu} u^\mu = -p_t \ , \\ L \equiv& m_\mu u^\mu = g_{\varphi\mu} u^\mu = p_\varphi \ , \end{aligned}$$

this is, conservation of energy and conservation of angular momentum with respect to the symmetry axis. In the last equality we have used the second concept: geodesic equation. The geodesic equation is equivalent to the Euler-Lagrange equation associated to a lagrangian $\mathcal{L} = \frac{1}{2} g_{\mu\nu} \dot{x}^\mu \dot{x}^\nu$, with the corresponing conjugate momentum $p_\mu = \partial\mathcal{L}/\partial\dot{x}^\mu = g_{\mu\nu}\dot{x}^\nu$. Using the Hamilton-Jacobi equation

$$H\left(x^\mu, \frac{\partial S}{\partial x^\mu}\right) + \frac{\partial S}{\partial \lambda} = 0 \ , \tag{3.6}$$

being $H = \frac{1}{2} g_{\mu\nu} \dot{p}^\mu \dot{p}^\nu$ the Hamiltonian, has the advantage that one can obtain an extra integral of motion by using the separability of the Boyer-Lindquist coordinates [29]. The Jacobi action S is therefore

$$S = -\frac{1}{2}\kappa\lambda - Et + L\varphi + S_{(r,\theta)}(r,\theta) = -\frac{1}{2}\kappa\lambda - Et + L\varphi + S_{(r)}(r) + S_{(\theta)}(\theta) \ ,$$

where we have assumed that the extra term of the action is separable and used $g_{\mu\nu}u^\mu u^\nu \equiv \kappa$. Inserting this ansatz in (3.6) and after some manipulation one obtains

$$\begin{aligned} \Delta\left(\frac{dS_{(r)}}{dr}\right)^2 - \kappa r^2 - \frac{(r^2+a^2)^2}{\Delta}E^2 + \frac{4Mra}{\Delta}EL - \frac{a^2}{\Delta}L^2 + a^2E^2 + L^2 = \\ = -\left(\frac{dS_{(\theta)}}{d\theta}\right)^2 + \kappa a^2\cos^2\theta + a^2\cos^2\theta E^2 - \cot^2\theta L^2 \ , \end{aligned}$$

such that the left hand side is r-dependent and the right hand side is θ-dependent, so each side must be equal to a constant $\mathcal{W}$. The equations are therefore

$$\begin{aligned} \frac{dS_{(r)}}{dr} &= \pm\frac{\sqrt{R(r)}}{\Delta} \ , \\ \frac{dS_{(\theta)}}{d\theta} &= \pm\sqrt{\Theta(\theta)} \ , \end{aligned}$$

where, defining $Q = \mathcal{W} - (L - aE)^2$,

$$R(r) = P^2 - \Delta(\kappa r^2 + \mathcal{W}) \ , \tag{3.7}$$

$$\Theta(\theta) = Q - \cos^2\theta\left[a^2(\kappa - E^2) + L^2\sin^{-2}\theta\right] \ , \tag{3.8}$$

$$P = E(r^2+a^2) - aL \ . \tag{3.9}$$

Finally, the Jacobi action reads

$$S = -\frac{1}{2}\kappa\lambda - Et + L\varphi \pm \int^{\theta} \sqrt{\Theta(\theta)}d\theta \pm \int^{r} \frac{\sqrt{R(r)}}{\Delta}dr. \tag{3.10}$$

Differentiating the Jacobi action with respect to the constants of motion gives a constant and therefore the integrals of motion are obtained by deriving with respect to $(\mathcal{W}, \kappa, E, L)$,

$$\int \frac{d\theta}{\pm\sqrt{\Theta(\theta)}} = \int \frac{dr}{\pm\sqrt{R(r)}}, \tag{3.11}$$

$$\lambda = \mp \int^{\theta} \frac{a^2\cos^2\theta}{\sqrt{\Theta(\theta)}}d\theta \mp \int^{r} \frac{r^2}{\sqrt{R(r)}}dr, \tag{3.12}$$

$$t = \mp \int^{\theta} \frac{a^2 E\cos^2\theta}{\sqrt{\Theta(\theta)}}d\theta \mp \int^{r} \frac{E(r^2+a^2)r^2 + 2Mar(L-aE)}{\Delta\sqrt{R(r)}}dr, \tag{3.13}$$

$$\varphi = \int^{\theta} \frac{L\sin^{-2}\theta}{\pm\sqrt{\Theta(\theta)}}d\theta + \int^{r} \frac{a(2MrE - aL)}{\pm\Delta\sqrt{R(r)}}dr. \tag{3.14}$$

Now we have four integrals of motion for four spacetime parameters for geodesics characterized by the set of parameters $(\mathcal{W}, \kappa, E, L)$.

3.3.1 Observer frame

In order to constrain what an observer in the Earth will see, first of all we have to define the observer's sky. In order to define the observer's sky we can make use of the fact that Boyer-Lindquist coordinates reduce to euclidean coordinates at infinity $r_o \to \infty$. As in [26], we will assume that the BH is rotating in the z-direction, with $a > 0$ being counterclockwise in the positive direction (see fig. 3.5) . The Boyer-Lindquist coordinates of the observer will be $(r_o, \theta_o, 0)$ and the source will be located at $(r_S, \theta_S, \varphi_S)$. The observer will see a photon coming

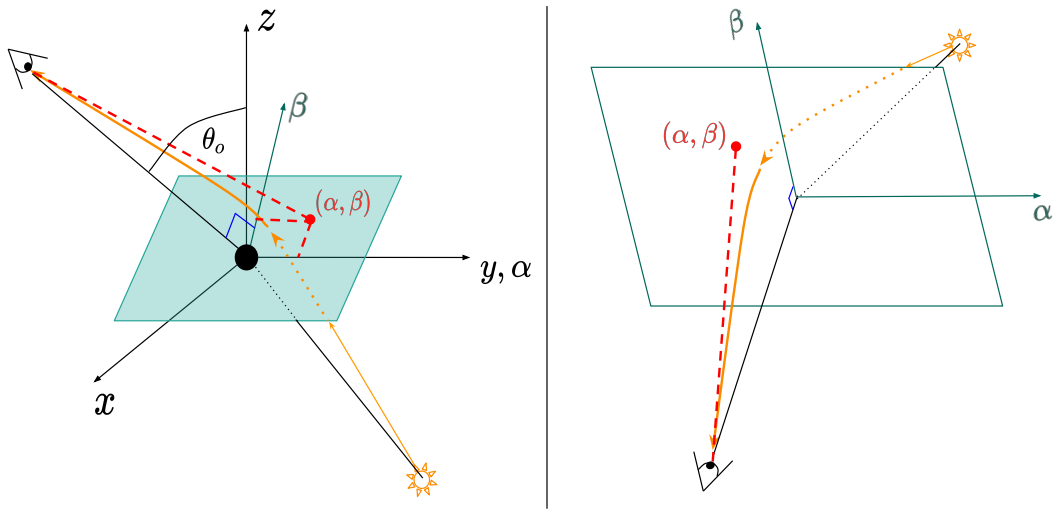

Figure 3.5: Geometry of the system. The observer's sky plane is perpendicular to the line joining the observer and the black hole.

in a straight line from the direction given by the tangent vector of the photon curve in the position r_o of the observer. This curve is parametrized by r such that $r^2 = x^2 + y^2 + z^2$. The

tangent vector $\vec{T}$ to the curve at the observer position is given by

$$\begin{aligned}\vec{T} &= \left(\left.\frac{dx}{dr}\right|_{r=r_o}, \left.\frac{dy}{dr}\right|_{r=r_o}, \left.\frac{dz}{dr}\right|_{r=r_o} \right) \\ &= \left(\sin\theta_o + r_o\cos\theta_o \left.\frac{d\theta}{dr}\right|_{r=r_o}, r_o\sin\theta_o \left.\frac{d\varphi}{dr}\right|_{r=r_o}, \cos\theta_o - r_o\sin\theta_o \left.\frac{d\theta}{dr}\right|_{r=r_o} \right) .\end{aligned}$$

The observer's sky is defined as the plane perpendicular to the line joining the observer and the black hole. The point at which the line intersects the plane is given by

$$\begin{aligned}(-\beta\cos\theta_o, \alpha, \beta\sin\theta_o) &= -r_o\vec{T} + (r_o\sin\theta_o, 0, r_o\cos\theta_o) = \\ &= \left(-r_o^2\cos\theta_o \left.\frac{d\theta}{dr}\right|_{r=r_o}, -r_o^2\sin\theta_o \left.\frac{d\varphi}{dr}\right|_{r=r_o}, r_o^2\sin\theta_o \left.\frac{d\theta}{dr}\right|_{r=r_o} \right), \quad (3.15)\end{aligned}$$

where in the first term we multiply by the magnitude of the vector and in the second term we add the location of the observer. From (3.15) we can directly read the coordinates in the observer's sky

$$\alpha = -r_o^2\sin\theta_o \left.\frac{d\varphi}{dr}\right|_{r=r_o} , \tag{3.16}$$

$$\beta = r_o^2 \left.\frac{d\theta}{dr}\right|_{r=r_o} . \tag{3.17}$$

In the following section we will relate the observer's sky coordinates to the parameters describing the geodesics.

3.3.2 Shadow of the black hole

In order to consider the case of a photon from infinity and lensed by the Kerr BH, and reaching an observer at infinity, we need to study null geodesics. Null geodesics ($E = 1$, $\kappa = 0$) are described by the following set of differential equations from the integrals of motion

$$\Sigma u^r = \pm\sqrt{R(r)} , \tag{3.18}$$

$$\Sigma u^\theta = \pm\sqrt{\Theta(\theta)} , \tag{3.19}$$

$$\Sigma u^\varphi = -\left(a - \frac{L}{\sin^2\theta} \right) + \frac{aP}{\Delta} , \tag{3.20}$$

$$\Sigma u^t = -a(a\sin^2\theta - L) + \frac{(r^2+a^2)P}{\Delta} . \tag{3.21}$$

The factor Σ can be absorbed in the affine parameter by using the Meno time $d\lambda = \Sigma d\lambda'$. In the Kerr black hole, because it is not spherically symmetric, the photons are not confined in a plane but accquire a precesion movement. Note that turning points are defined by $u^\mu = dx^\mu/d\lambda = 0$ and therefore the radial turning point $r_{\min}$ will be the largest positive root of $R(r) = 0$, while the angular turning points $(\theta_{\min}, \theta_{\max})$ are the roots of $\Theta(\theta) = 0$. The photon reaching the observer therefore moves in the following order $r_S \to r_{\min} \to r_o$ and $\theta_S \to \theta_{\min/\max} \to \theta_{\min/\max} \to \cdots \to \theta_o$.

Using the set of differential equations we can derive a relation between the parameters of the geodesic and the observer's sky coordinates. Using that $d\varphi/dr = u^\varphi/u^r$ and $d\theta/dr = u^\theta/u^r$, and taking the limit $r_o \to \infty$ we obtain a relation between the observer's sky coordinates and the conserved quantities characterizing the geodesics

$$\alpha = -\frac{L}{\sin\theta_o} , \tag{3.22}$$

$$\beta = \pm\sqrt{Q + a^2\cos^2\theta_o - L^2\cot^2\theta_o} . \tag{3.23}$$

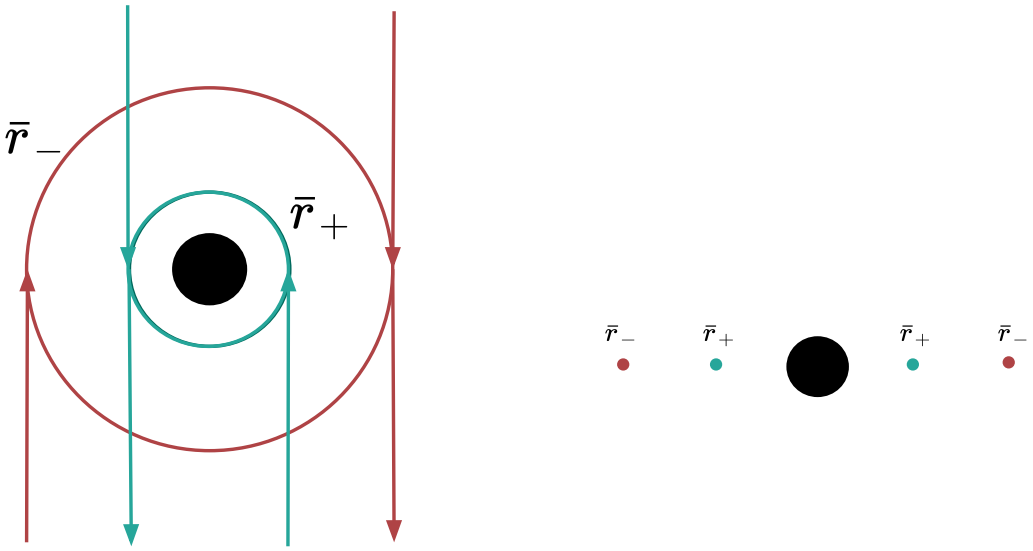

(a) View perpendicular to the equatorial plane $(x, y, 0)$ in Boyer-Lindquist coordinates, the spin is pointing outwards the plane.

(b) Equatorial view.

Figure 3.6: Pictorial representation of the turning points $[\bar{r}_+, \bar{r}_-]$ for unstable orbits and the way the photons reach the observer, i.e., twisting around the black hole and eventually escaping to infinity. In this case we are showing photons coming from the observer side and behind the black hole, but actually the photons coming to the equatorial plane can come from any direction due to the unstable nature of the orbit.

Since the geodesics are parametrized by L and Q (or equivalently L and $\mathcal{W}$), is useful to explore the region of the parameter space (L, Q) at which photons that reach $r_{\rm min}$ can escape to infinity [26]. Rewriting (3.19) as

$$u^{\theta\,2} = Q + a^2\cos^2\theta - L^2\cot^2\theta \ ,$$

and considering a photon crossing the equator $\theta = \pi/2$, we obtain $Q = u^{\theta\,2} \geq 0$. Taking into account photons that return to infinity means that $du^r/d\lambda > 0$ at $r = r_{\rm min}$, i.e., moving away from the BH. Hence, in order to know the limiting case, we set $u^r|_{r=\bar{r}} = 0$ and $du^r/d\lambda|_{r=\bar{r}} = 0$, with $\bar{r}$ being the lower bound of $r_{\rm min}$. With these conditions we are able to solve Q and L in terms of $\bar{r}$

$$L(\bar{r}) = \frac{\bar{r}^2(\bar{r} - 3M) + a^2(M + \bar{r})}{a(M - \bar{r})} \ , \tag{3.24}$$

$$Q(\bar{r}) = \frac{r^3\left(4a^2M - r(r - 3M)^2\right)}{a^2(M - r)^2} \ . \tag{3.25}$$

The limiting case $Q = 0$ yields two roots for $\bar{r}$ outside the event horizon namely $\bar{r}_+$ and $\bar{r}_-$. These roots are computed for a photon in the equator. In order to get some physical insight we can substitute these roots in $L(\bar{r})$, where we obtain $L(\bar{r}_+) > 0$ and $L(\bar{r}_-) < 0$, so we have two different turning points: $\bar{r}_+$ for photons moving with positive angular momentum, i.e., rotating in the same sense as the black hole; and $\bar{r}_-$ for photons moving with negative angular momentum, counter-rotating with respect to the black hole [26]. In fig. 3.6a we see a polar view of the trajectory of photons coming from the observer side (bottom) that turn around and

return to the observer; and photons coming from the opposite side which reach the observer from the same point. In fig. 3.6b we see these points from the equatorial plane. From equation (3.23) we can see that for photons to reach an observer, the argument inside the square root must be positive or equal to zero. In the case of an observer in the equatorial plane the condition reduces to $Q \geq 0$, so the values $r \in (\bar{r}_+, \bar{r}_-)$ correspond to photons reaching the equatorial plane from all different inclinations. In the case that the observer is not in the equatorial plane the condition for a photon to reach her/him is given by $Q + a^2 \cos^2\theta - L^2 \cot^2\theta \geq 0$, which roots will be smaller than $[\bar{r}_+, \bar{r}_-]$.

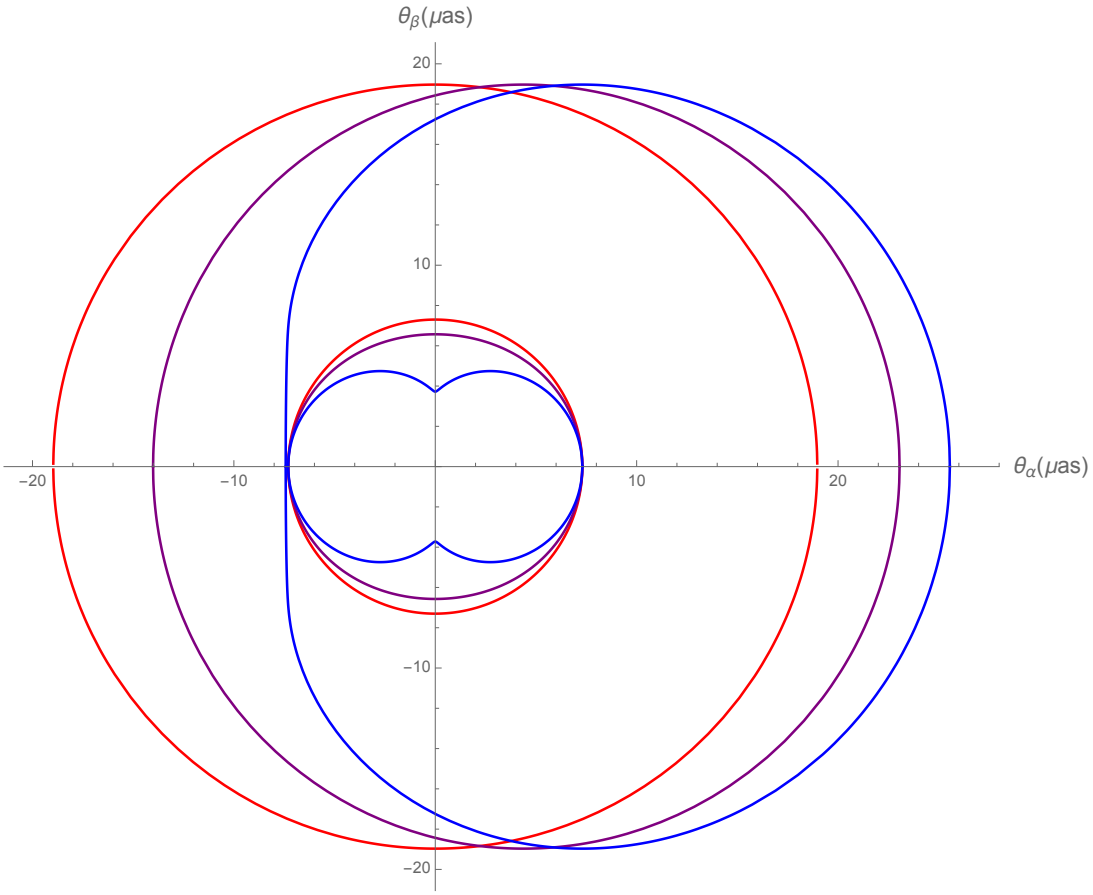

Figure 3.7: Shadow of the Kerr black hole (outer curve) and black hole ergoregion (inner curve). This corresponds to the black hole located at M87 with $M = 6.2 \times 10^9 M_\odot$ and $r_o = 16.8$Mpc for an equatorial observer. The red corresponds to $a = 0$, the purple is $a = 0.6M$ and blue is $a = 0.9998M$.

Using basic geometry we can obtain the angular distances from α and β as $\alpha \simeq r_o\theta_\alpha$ and $\beta \simeq r_o\theta_\beta$. The curve in the parametric space $(\theta_\alpha(\bar{r}), \theta_\beta(\bar{r}))$ is called the shadow of the black hole and gives the limiting shape of the black hole seen by an observer (see fig. 3.7). This shape is flattened in the side corresponding to the rotation of the black hole facing the observer. As we argued before, this is because the turning points depend on the angular momentum of the photons, differentiating between photons co-rotating and counter-rotating with the black hole.

Chapter 4

Measuring the ultralight boson mass

Let us assume that we are able to observe a Kerr black hole in presence of an ultralight boson field and with no external processes like accretion disks. We can have two cases corresponding to the superradiance amplification or to an exponential supression of the field. The latter case, contrary to the former, will not be of interest since it will not affect the dynamics of the black hole. In the superradiance regime, as discussed in chapter 2, the black hole will lose up to a 10% of its mass and a considerably large percentage of spin. The gravitational lensing of light by the black hole (discused in chapter 3) will be affected by the dynamics of the superradiant process, leading to a characteristic observational signature. In this chapter we will compute the spin evolution of the black hole and relate it to the shadow of the black hole seen by an observer due to gravitational lensing. Later we will discuss the different possibilites of observation depending on different scenarios and finally we will discuss the combination with multi-messenger astronomy.

4.1 Spin and mass evolution

In order to know the observational properties of the superradiant instability we have to take into account the change in the BH mass and spin. Therefore, we will study how the spin and mass evolves with time and relate this to the shadow of the BH. In order to do so we will use the equations derived in sec. 2.1. Ignoring external processes such as accretion, the differential equations descriving the evolution of the system are [23]

$$\frac{dJ}{dt} = -\frac{dJ_c}{dt} \ , \tag{4.1a}$$

$$\frac{dJ_c}{dt} = -\frac{l}{\mu}\frac{dE_c}{dt} \tag{4.1b}$$

$$\frac{dE_c}{dt} = \frac{dM_c}{dt} \ , \tag{4.1c}$$

$$\frac{dM}{dt} = -\frac{dM_c}{dt} \ . \tag{4.1d}$$

Now, in order to compute the energy of the cloud we will use the strategy followed in ref. [30], i.e., relate the flux of energy through the horizon with the time evolution of the field. For doing so, we take into account the killing vector associated to the time coordinate $\xi^\mu = (1, 0, 0, 0)$ such that

$$\nabla_\mu (T^\mu{}_\gamma \xi^\gamma) = \nabla_\mu T^\mu{}_0 = 0.$$

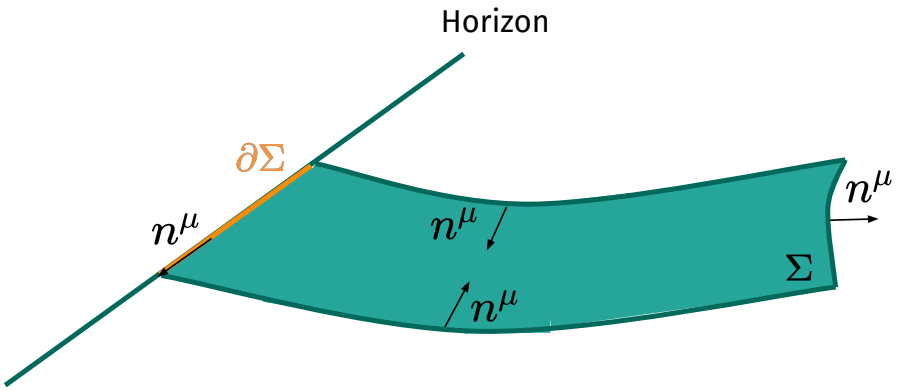

Figure 4.1: Four-volume considered for the energy flux. The two spacelike hypersurfaces tend to 0 when taking $\Delta t \to 0$. We also show the correct direction of the normal vector to each surface (null at the horizon, ingoing on the sides and outgoing at infinity).

The way to relate the flux in the horizon to the time evolution of the field is considering a semi-infinte four-volume formed by two spacelike hypersurfaces separated by Δt and closed by a timelike hypersurface at infinity and the BH event horizon. Then applying Gauss' law and taking $\Delta t \to 0$ the integrals of the spacelike hypersurfaces cancel and therefore

$$\frac{dE}{dt} = \int_{\partial\Sigma} d\Omega T^\mu{}_0 k_\mu = -\frac{\partial}{\partial t}\left(\int_\Sigma d^3x T^\mu{}_0 n_\mu\right) , \tag{4.2}$$

where

$$n^\mu = -(1, 0, 0, \Omega_H) \tag{4.3}$$

is the normal vector pointing outside the surface. Since the only time-dependent part in the scalar energy-momentum tensor is $\phi^2 \propto e^{2\Gamma_{nlm}t}$, the right hand side will pick up an overall factor of $2\Gamma_{nlm}$. Therefore,

$$\frac{dE}{dt} = -2\Gamma_{nlm}\left(\int_\Sigma d^3x T^\mu{}_0 n_\mu\right) = -2\Gamma_{nlm} M_c$$

where in the last step we have used the definition of the mass of the cloud. Using that the change of the energy of the cloud is at expenses of a change of the energy of the black hole, $dE/dt = -dE_c/dt$, we get

$$\frac{dE_c}{dt} = 2\Gamma_{nlm} M_c \ . \tag{4.4}$$

Now we can solve the system of differential equations numerically. For that, we have to choose an initial value of the mass of the cloud. Following [31], we will take different initial values (or *seeds*) corresponding to different situations. The different seeds are $M_{c,0} = 10^-9 M_0$, being M_0 the initial mass of the black hole, corresponding to a very small number of particles in the cloud or alternatively to quantum fluctuations near the BH; and $M_{c,0} = 0.025 M_0$, which correspond to astrophysical scenarios where the BH is formed in presence of the cloud (either by collapse or by a binary merger with a cloud). The results for an ultralight boson $\mu = 7 \times 10^{-12}$eV and a black hole with $M_0 = 6 M_\odot$ and $J_0/M_0^2 = 0.8$ are shown in fig. 4.2. In order to cross-check our code, we compared results with refs. [23] and [31]. We see that for the smallest seed the time necessary for the cloud to grow and trigger the instability is roughly 10 times the superradiant time-scale (it is the case for other choices of parameters such as the one in the references refered

above), which makes sense if we think about the small initial number of particles. On the other hand, for the astrophysical seed, we see that the spindown happens within the superradiant time-scale (in this case is given by 1.5yr) and in both cases the final spin and mass of the black hole are the same. In order to relate the spindown to the mass of the ultralight boson

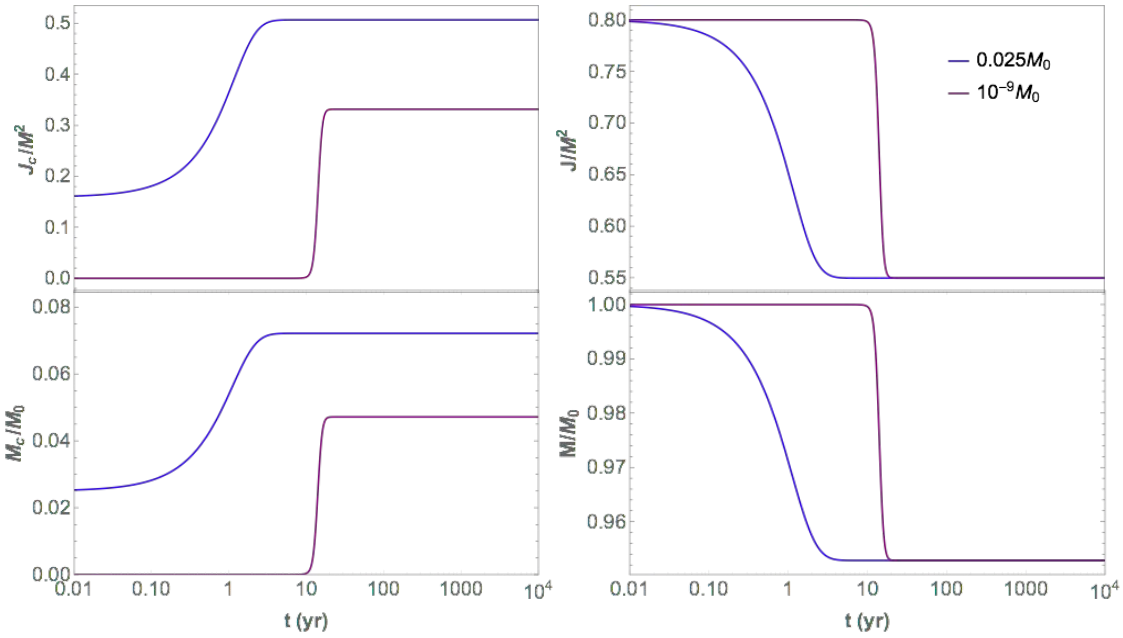

Figure 4.2: Spin evolution for the case of an ultralight boson $\mu = 7 \times 10^{-12}$eV and a black hole with initial mass $M_0 = 6M_\odot$ and initial spin $J_0/M_0^2 = 0.8$ for different seeds. The left and right columns correspond to the spin and mass of the cloud and the black hole respectively.

and other system parameters we will use an ansatz and by means of the differential equations governing the system we will obtain a fitting formula. By looking at the evolution for different seeds wee see that for seeds larger than $M_{c,0} = 0.5M_0$ the evolution is well described by

$$J(t) = (J_0 - J_f)\exp(-\gamma_J t) + J_f \ , \qquad \gamma_J = \frac{2l\Gamma_{nlm,0}M_{c,0}}{\mu(J_0 - J_f)} \ , \tag{4.5}$$

$$M(t) = (M_0 - M_f)\exp(-\gamma_M t) + M_f \ , \qquad \gamma_M = \frac{2\Gamma_{nlm,0}M_{c,0}}{(M_0 - M_f)} \ , \tag{4.6}$$

whereas for seeds $0.5M_0 > M_{c,0} \geq 0.01M_0$ the evolution is more drastic and is well described by

$$J(t) = (J_0 - J_f)\exp\left(-\gamma_J t - \beta_J t^2\right) + J_f \ , \quad M(t) = (M_0 - M_f)\exp\left(-\gamma_M t - \beta_M t^2\right) + M_f \ , \tag{4.7}$$

$$\beta_{J/M} = \frac{\log(2)}{t_*^2} - \frac{\gamma_{J/M}}{t_*} \ , \qquad t_* = \frac{2}{\gamma_J}\frac{M_{c,0}}{M_{c,f} + M_{c,0}} \ ,$$

where the subscript f denotes the value at the final state of the evolution and t_* is the half-time of the evolution (see appendix D).

4.2 Black hole shadow

As we have seen in sec. 3.3.2, the shape of the shadow of the black hole is very sensitive to the spin of the black hole. In this section we will further explore the properties of the black hole

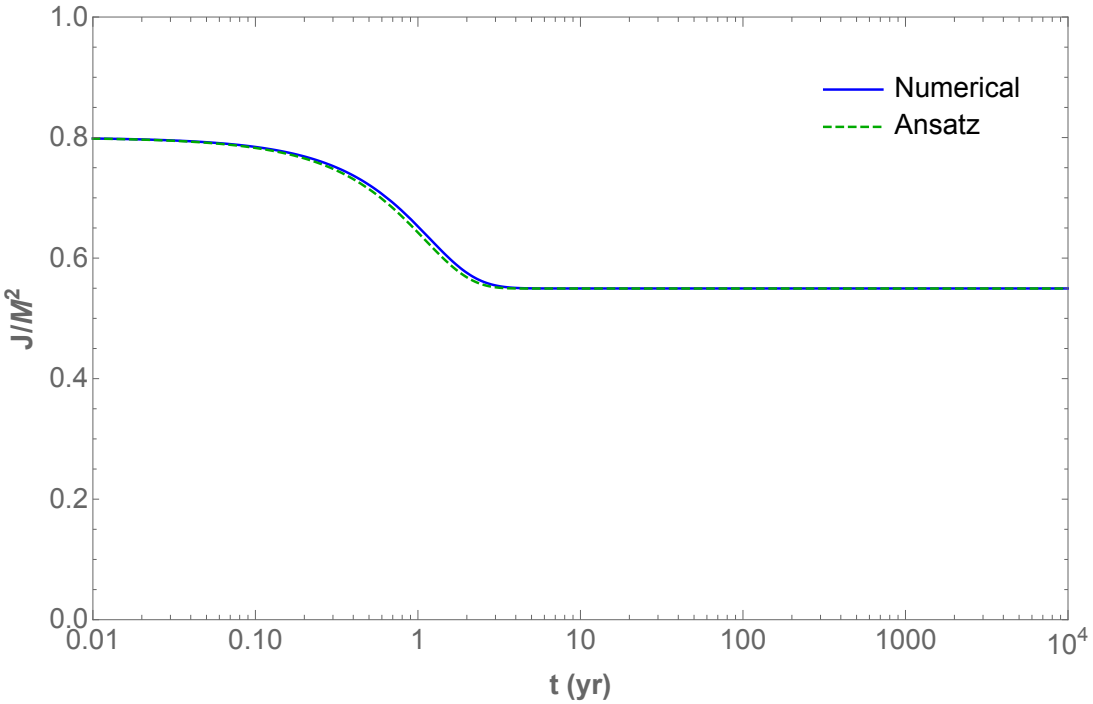

Figure 4.3: Evolution of the spin of the black hole with time. The solid line represents the numerical solution to the set of differential equations (4.1) and the dashed line is the semi-analytic solution (4.7) for a seed of $M_{0,c} = 0.025M_0$. We see that is a good approximation. This plot corresponds to an ultralight boson $\mu = 7 \times 10^{-12}$eV and a black hole with $M_0 = 6M_\odot$ and $J_0/M_0^2 = 0.8$.

shadow and relate the angular diameter to the spin of the black hole.

In sec. 3.3.2 we provided a derivation of the shadow of the black hole for an observer orientation of $\theta_o = \pi/2$. Recall that in order to obtain the shadow for arbitrary orientations one has to solve the equation $Q + a^2\cos^2\theta - L^2\cot^2\theta = 0$ and then compute both the constants of motion and the maxium approach distance $\bar{r}$ in order to obtain the parametric curve $(\theta_\alpha(\bar{r}), \theta_\beta(\bar{r}))$. Since the shape of the shadow changes more significantly along the line $\theta_\beta = 0$, we define the (angular) diameter of the shadow d_{sh} as

$$d_{sh} = \frac{1}{r_o}\left(|\theta_\alpha(\bar{r}_+)| + |\theta_\alpha(\bar{r}_-)|\right) \ , \tag{4.8}$$

with $\bar{r}_{+/-}$ being the maximum approach distance for prograde and retrogade photons. We have chosen this particular direction because it is the one that changes the most with the spin. Since $\bar{r}_{+/-}$ cannot be expressed in a simple way (at least for any value of the spin, mass and observer inclination) we have computed it numerically. If we consider a black hole like M87 (although the discussion is valid for any BH), the shadow diameter of the black hole changes with spin as is showed in figure 4.4. We see that, due to the axial symmetry, the diameter seen by an observer in the polar plane $\theta_o = 0$ change less than the diameter seen by an equatorial observer, where the deformation is maximal.

In ultimate instance we want to relate the shadow diameter to the spin of the black hole analytically. In order to find an approximate solution we have assumed that the shadow diameter changes as a power function

$$d_{sh} \simeq A + B\left[1 - \left(\frac{a}{M}\right)^2\right]^\delta \ , \tag{4.9}$$

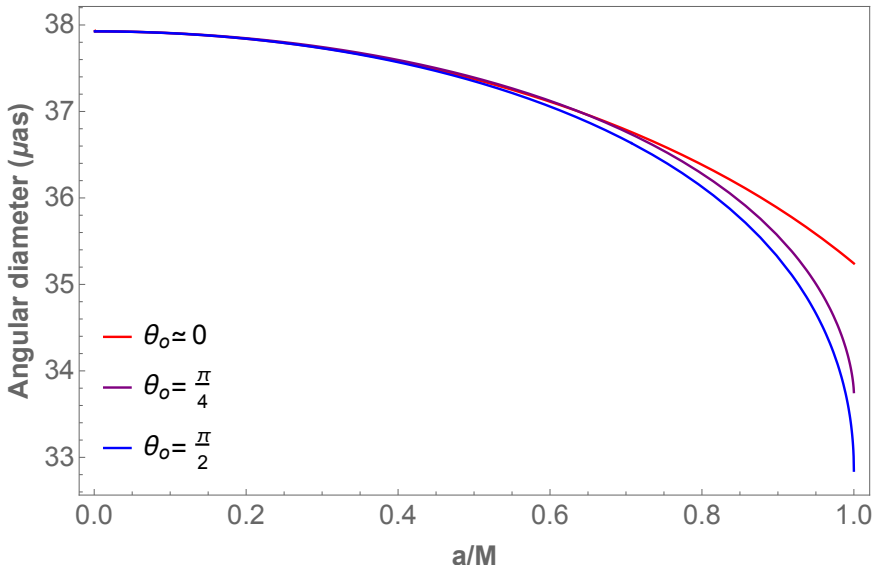

Figure 4.4: Angular diameter of the BH shadow for different observer inclinations. This corresponds to the black hole located at M87 with $M = 6.2 \times 10^9 M_\odot$ and $r_o = 16.8$Mpc.

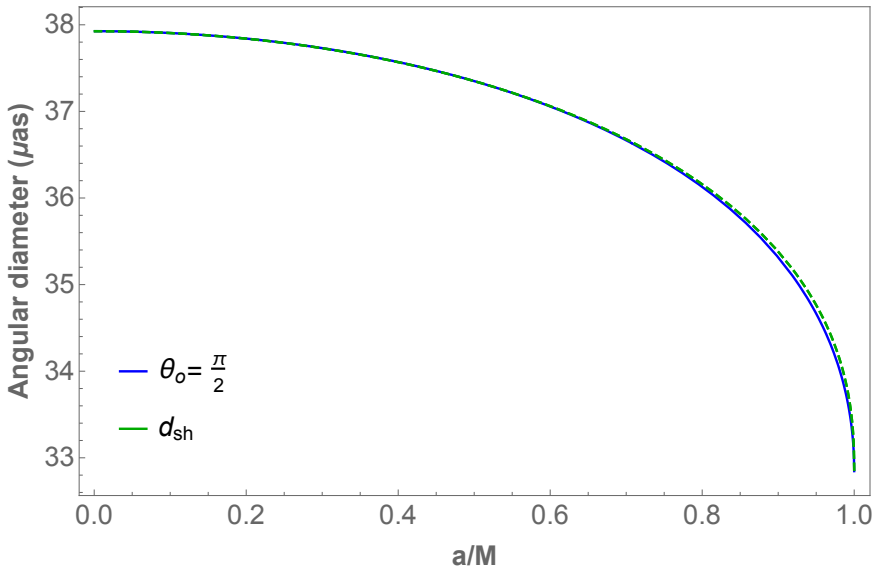

Figure 4.5: Plot of the shadow diamater using the analytical formula (dashed) and the numerical value.

where we have assumed that the spin must be squared because the shadow diammeter must be invariant under the symmetry $a \to -a$. Assuming an observer in the equatorial plane (since the shadow diameter is similar to an observer at intermediate orientations) the easiest cases to compute analytically are the ones for $a = 0$, $a = 0.5M$ and $a = M$ in such a way that we are able to solve for each coefficient (see appendix E). The equation for the shadow diameter

reads

$$d_{sh} = \frac{3M}{r_o}\left\{3 + (2\sqrt{3}-3)\left[1 - \left(\frac{a}{M}\right)^2\right]^{\delta}\right\} , \tag{4.10}$$

with

$$S \equiv \sin\left(\frac{\pi}{9}\right) + \sin\left(\frac{2\pi}{9}\right) , \qquad \delta = \frac{\log\left(\frac{2\sqrt{3}-3}{2\sqrt{3}S-3}\right)}{\log(4/3)} .$$

For comparison, in figure 4.5 we plot d_{sh} with the numerical calculations and we see that it provides a solid approximation. Now we can express the spin in terms of the shadow diameter inverting eq. (4.10)

$$\frac{a}{M} = \pm\sqrt{1 - \left(\frac{\frac{r_o d_{sh}}{3M} - 3}{2\sqrt{3}-3}\right)^{1/\delta}} , \tag{4.11}$$

such that we can directly relate the measured shadow diameter of the black hole to the spin, which will be used in the next sections.

4.3 Observational properties and measuring strategy

As we have seen in chapter 2, the time-scales and evolution of the Gravatom are of extremely importance for observational purposes. A realistic astronomical observation time is of the order of 5 yr, which can coincide with the spindown time-scale due to superradiance instability for a suitable choice of parameters, namely the black hole mass and the boson mass. In an optimistic scenario we would be able to observe a spinning down black hole due to a superradiance instability with a time-scale from 1 to 10 years. An example of this is the case of a $6M_\odot$ BH and an ultralight boson mass $\mu = 0.7 \times 10^{-11}$eV that we have discussed in sec. 2.3, where the time-scale was of 1.5 years.

The mass of the black hole - mass of the boson parameter space satisfying $\alpha < 0.5$ and a superradiance time-scale below 10 years is plotted in fig. 4.6 for modes l from 1 to 3 and spins between $a = 0.5M$ and $a = M$. Although fig. 4.6 refers to a superradiance time-scale, we have to take into account the spin evolution of the system. Looking at fig. 4.3 we see that the spindown of the black hole changes before superradiance finishes. In order to give an estimation of the time at which the system changes fast enough to be observable, we will use eq. (4.7) and define the *observation time*, t_{obs} as the e-folding time of the evolution

$$t_{obs} = \frac{\gamma}{2\beta}\left(\sqrt{1 - \frac{4\beta}{\gamma^2}} - 1\right) , \tag{4.12}$$

where we have assumed that the seeds are of astrophysical origin (i.e. $0.5M_0 > M_{c,0} \geq 0.01M_0$). Within this observation time, as plotted in fig. 4.7, we can observe a fast spin-down of black holes of mass $M \sim M_\odot - 10^7 M_\odot$ associated to a boson mass of $\mu \sim 10^{-17}\text{eV} - 10^{-10}\text{eV}$ starting from an initial spin between $a = 0.5M - M$, and for the modes $l = 1, 2, 3$.

The observational strategy is the following:

- Observation of the spindown of a Kerr black hole due to superradiant instability for a period from 1 to 10 years.
- Measurement of the shadow of the black hole in the observer's sky.
- Relate this change to a change in the spin of the black hole.
- Compute the superradiance time-scale and solve for the fastest mode.

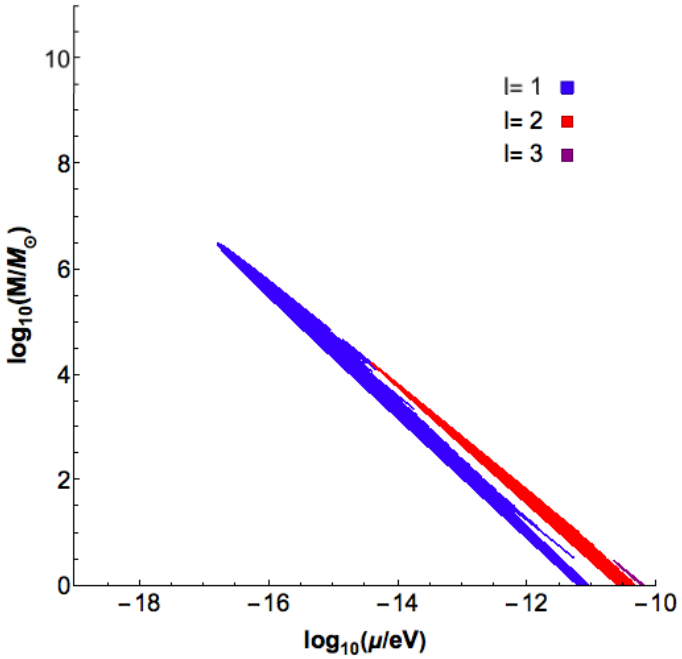

Figure 4.6: Parameter space satisfying $\alpha < 0.5$ and a superradiance time-scale from 1 to 10 years for $l = 1, 2, 3$ and $a = 0.5M, ..., M$. Higher number of modes l are discarded.

- Compute the mass of the ultralight boson.

Assuming the fastest level $l = m$ and a radial quantum number $n = 0$ (recall that the dependence in the radial quantum number n is mild. Here we choose $n = 0$ because it is a value that maximizes the superradiant rate up to, at least, $l = 3$ [6]), the equations that we will use to solve the system are

$$\Gamma_{0ll} = -2\frac{r_+}{r_g}(\mu - m\Omega_H)\alpha^{4l+5}\frac{2^{4l+2}(2l+1)!}{(l+1)^{2l+4}}\left[\frac{l!}{(2l)!(2l+1)!}\right]^2 \times \times \prod_{k=1}^{l}\left[k^2\left(1-\chi^2\right) + 4r_+^2(\mu - m\Omega_H)^2\right] , \tag{4.13}$$

$$\mu = \frac{l}{2r_{g,f}}\frac{a_f}{r_{+,f}} = \frac{l}{2r_{g,f}}\frac{\chi_f}{\left(1+\sqrt{1-\chi_f^2}\right)} , \tag{4.14}$$

$$\alpha_f = \frac{l^3}{8\alpha_0\left(l-\alpha_0\chi_0\right)}\left[1 - \sqrt{l - \frac{16\alpha_0^2\left(1-\alpha_0\chi_0\right)^2}{l^3}}\right] , \tag{4.15}$$

$$M_{c,f} = M_{c,0} + M_0 - M_f , \tag{4.16}$$

$$\chi(t) = (\chi_0 - \chi_f)\exp\left(-\gamma t - \beta t^2\right) + \chi_f , \tag{4.17}$$

$$\gamma = \frac{2l\Gamma_{nlm,0}M_{c,0}}{\mu(J_0 - J_f)} , \tag{4.18}$$

$$\beta = \frac{\log(2)}{t_*^2} - \frac{\gamma}{t_*} , \tag{4.19}$$

$$t_* = \frac{2}{\gamma}\frac{M_{c,0}}{M_{c,f} + M_{c,0}} . \tag{4.20}$$

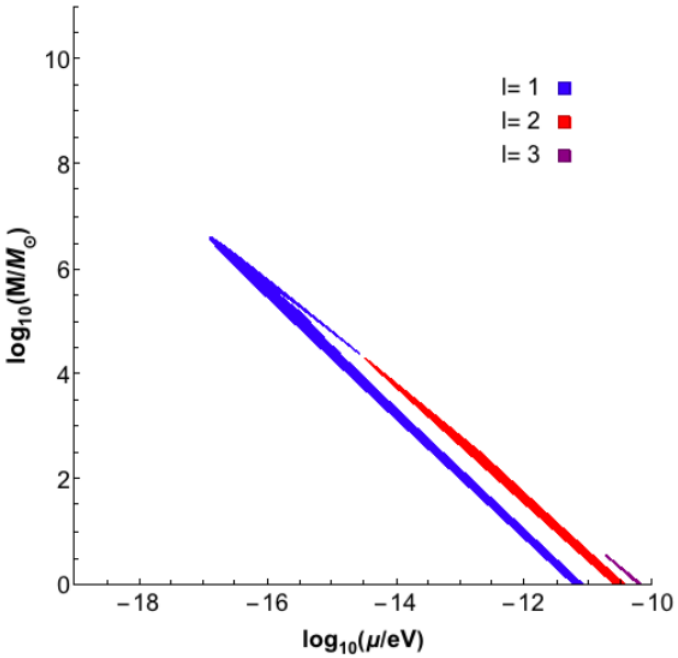

Figure 4.7: Parameter space satisfying $\alpha < 0.5$ and an observation time-scale from 1 to 10 years for $l = 1, 2, 3$ corresponding to the blue, red and purple regions respectively, and $a = 0.5M, ..., M$. The values inside the colored region are observable within 1 to 10 years, where higher modes were discareded, meaning that they don't belong to the parameter space for this range of observation time. The lines are consequence of the quantized behavior of the boson.

where we have defined $\chi \equiv a/r_g$ and t_* is the half-time of the evolution. Relating the shadow angular diameter with the spin allow us to compute the evolution of spin with time. From eqs. (4.17) and (4.19),

$$\gamma = \frac{\log\left(\frac{J_o - J_f}{J(t) - J_f}\right) t_*^2 - \log(2) t^2}{t_* t (t_* - t)} \ , \tag{4.21}$$

where all the parameters are measurable. Using the equation for γ, eq. (4.18), we get

$$\frac{\Gamma_{0ll,0}\ l\ M_{c,0}}{\mu} = \frac{J_0 - J_f}{2} \frac{\log\left(\frac{J_o - J_f}{J(t) - J_f}\right) t_*^2 - \log(2) t^2}{t_* t (t_* - t)} \ . \tag{4.22}$$

Now, inserting eq. (4.14) into eqs. (4.13) and (4.22), and taking initial values, i.e. $\chi = \chi_0$ and $M = M_0$, we obtain

$$\begin{aligned} \Gamma_{0ll,0} = &- r_{+,0} \left(\frac{\chi_f}{r_{+,f}}\right)^{4l+5} \left(\frac{\chi_f}{r_{+,f}} - \frac{\chi_0}{r_{+,0}}\right) M_0^{4l+4} \frac{l^{4l+6}(2l+1)!}{2^3 (l+1)^{2l+4}} \left[\frac{l!}{(2l)!(2l+1)!}\right]^2 \times \\ &\times \prod_{k=1}^{l} \left[k^2 \left(1 - \chi_0^2\right) + l^2 {r_{+,0}}^2 \left(\frac{\chi_f}{r_{+,f}} - \frac{\chi_0}{r_{+,0}}\right)^2\right] \ , \end{aligned} \tag{4.23}$$

$$2\Gamma_{0ll,0} M_{c,0} \frac{r_{g,f}}{\chi_f} \left(1 + \sqrt{1 - \chi_f^2}\right) = \frac{J_0 - J_f}{2} \frac{\log\left(\frac{J_o - J_f}{J(t) - J_f}\right) t_*^2 - \log(2) t^2}{t_* t (t_* - t)} \ . \tag{4.24}$$

In order to compute the initial mass of the cloud $M_{c,0}$ we will use the equations for γ and β and the fact that the final mass of the cloud is given by the difference of the black hole mass

before and after superradiance, eq. (4.16). Using eqs. (4.18) and (4.19) we obtain

$$\frac{\gamma^2}{\beta} = \frac{4M_{c,0}^2}{M_{c,f}\log(2) + M_{c,0}(\log(2)-2)} \frac{1}{M_{c,f}+M_{c,0}} \,. \tag{4.25}$$

Using eq. (4.16) and solving the second order polynomial we obtain that the initial mass of the cloud reads

$$M_{c,0} = (M_f - M_0) \frac{\gamma\left\{\sqrt{4\beta\log(2)+\gamma^2} + \gamma\left[2\log(2)-1\right]\right\}}{4\gamma^2\left[\log(2)-1\right]-4\beta} \,, \tag{4.26}$$

where we are assuming that both the initial and final mass of the black hole are measurable by methods other than measuring the shadow diameter (we will expand on this in sec. 4.4). Once we know the initial mass of the cloud we can substitute it in eq. (4.24) such that we can compute $\Gamma_{l-1,l,l}$ and use eq. (4.23) in order to solve (numerically, using for instance the function FindRoot of Mathematica) for the mode l. Once we know the mode l we can solve for the mass of the ultralight boson using eq. (4.14).

4.4 Observation with multi-messenger astronomy

Multi-messenger astronomy is the combination of different astronomy messengers: electromagnetic radiation, gravitational radiation, cosmic rays and neutrinos. These messengers differ in the way they carry information (for instance gravitational waves and neutrinos pass through matter) and are associated to different processes within the same source [32]. One of the latest examples of multi-messenger observation is the observation of a binary neutron star merger, which was detected both in the gravitational wave and electromagnetic band [33]. Taking into account the gravitational wave signal of the system we can propose a scenario at which we can use both messengers (gravitational radiation and electromagnetic radiation) in order to observe and measure the black hole parameters as well as the ultralight boson mass.

4.4.1 Example: Black hole binary merger

One of the most challenging parts about studying a black hole is detecting it. To the date, the available ways of detecting a black hole are from studying the motion of nearby stars, study the position of stars changing by gravitational lensing or detecting X-rays from the presence of an accretion disk. Now, recent detection of gravitational waves open up the possibility to detect a black hole by the gravitational wave signature. In particular we have detected not only black hole binary mergers but also, as mentioned before, neutron star binary mergers. Nowadays the location of the gravitational wave source in the sky is a challenging task since we count with two gravitational wave observatories. With new incorporations to the gravitational wave detectors family such as KAGRA or IndiGO we would be able to infer the location of the source accurately. Gravitational wave detectors alongside VLBI (very-long baseline interferometers) or even SVLBI (space VLBI) provide a good array of multi-messenger observers. In order to carry out the multi-messenger observation we propose the following strategy:

- Gravitational wave detection of a black hole binary merger
- Computation of the source position
- Observation with VLBI or SVLBI
- Measure of the shadow diameter during the spindown
- Measure of the gravitational wave signal due to level transitions
- Measure of the gravitational wave signal due to cloud depletion after the spindown

This would allow us to cross-check results with multi-messenger astronomy. For complex fields, the gravitational wave emission can be supressed for certain configurations [9]. Measuring the instability by gravitational lensing would allow us to study these configurations. As an example let's take one of the gravitational wave detections, in particular the detection GW170729 [34]: a $50.6^{+16.6}_{-10.2}M_\odot$ and $34.3^{+9.1}_{-10.1}M_\odot$ black hole binary merger with a final black hole of mass $M = 80.3^{+14.6}_{-10.2}M_\odot$ and spin $a/M = 0.81^{+0.08}_{-0.13}$ at a distance $r_o = 2750^{+1350}_{-1320}$Mpc. Let us fix an ultralight boson mass of $\mu = 1.5\times10^{-13}$eV. In the following example we will use the parameters summarized in table 4.1. This combination of messengers can provide, for instance, the mass of the black hole independently of measuring the shadow, therefore making us able to compute the spin and solve the system or simply cross-check measurements. Although in order to observe

Parameter	**Value**
Initial mass of the black hole	$M_0 = 80M_\odot$
Initial spin of the black hole	$J_0/M_0^2 = 0.80$
Mass of the ultralight boson	$\mu = 1.5 \times 10^{-13}$eV
Mode	$l = 1$
Mass coupling	$\alpha = 0.089$
Distance from the observer	$r_o = 2750$Mpc
Observer orientation	$\theta_o = \pi/2$
Superradiant time-scale	$t_{sr} = 4.92$yr
Observation time-scale	$t_{obs} = 3.1$yr

Table 4.1: Parameters associated to the example. The superradiant and observation time-scales are computed from fixing the mass of the ultralight boson.

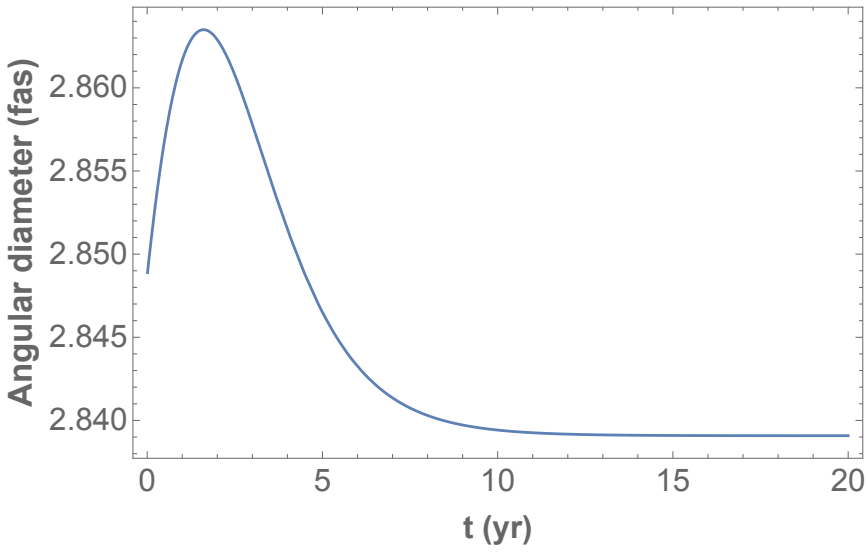

Figure 4.8: Evolution of the shadow diameter with time for the mentioned black hole.

this black hole we need an angular resolution of 10^{-15}arcsecond due to the large distance, this provides a good example of an observable spindown case. We could use our fitted formulas

but, in order to be as accurate as possible, we will use the numerical solutions to have an idea of what an observer would see. In fig. 4.8 we present the evolution of the shadow angular diameter with time and in fig. 4.9 we present how it would look like to an observer in Earth.

We see that the fact that both the mass and spin change, for this case, makes the shadow angular diameter expand and shrink, contrary to the intuitive picture that the shadow would increase by the spindown. We can explain this behavior by computing the time derivative of the shadow diameter,

$$\frac{d}{dt}\left(d_{sh}\right) = \frac{d}{dM}\left(d_{sh}\right)\frac{dM}{dt} + \frac{d}{dJ}\left(d_{sh}\right)\frac{dJ}{dt} = -2\Gamma_{nlm}M_c\left(\frac{d}{dM}\left(d_{sh}\right) + \frac{l}{\mu}\frac{d}{dJ}\left(d_{sh}\right)\right) \ .$$

We see that since the prefactor $2\Gamma_{nlm}M_c$ is always positive in the superradiant instability, what is happening is that the shadow in the begining changes faster with the spin (note that the spin can change more than a 50%) while the mass did not change much. As time goes on, the change in mass becomes noticeable and wins the competition against the change in spin. If we look at our fitted formula for the shadow diameter, eq. (4.10), we see that the spin has a term inversely proportional to the mass, therefore making a little change in mass noticeable when the spin cannot balance the rate anymore.

As discussed before, being able to observe the spindown of the BH and measure the shadow diameter will allow us to compute the mass of the ultralight boson, therefore enlightening, for instance, the dark matter problem.

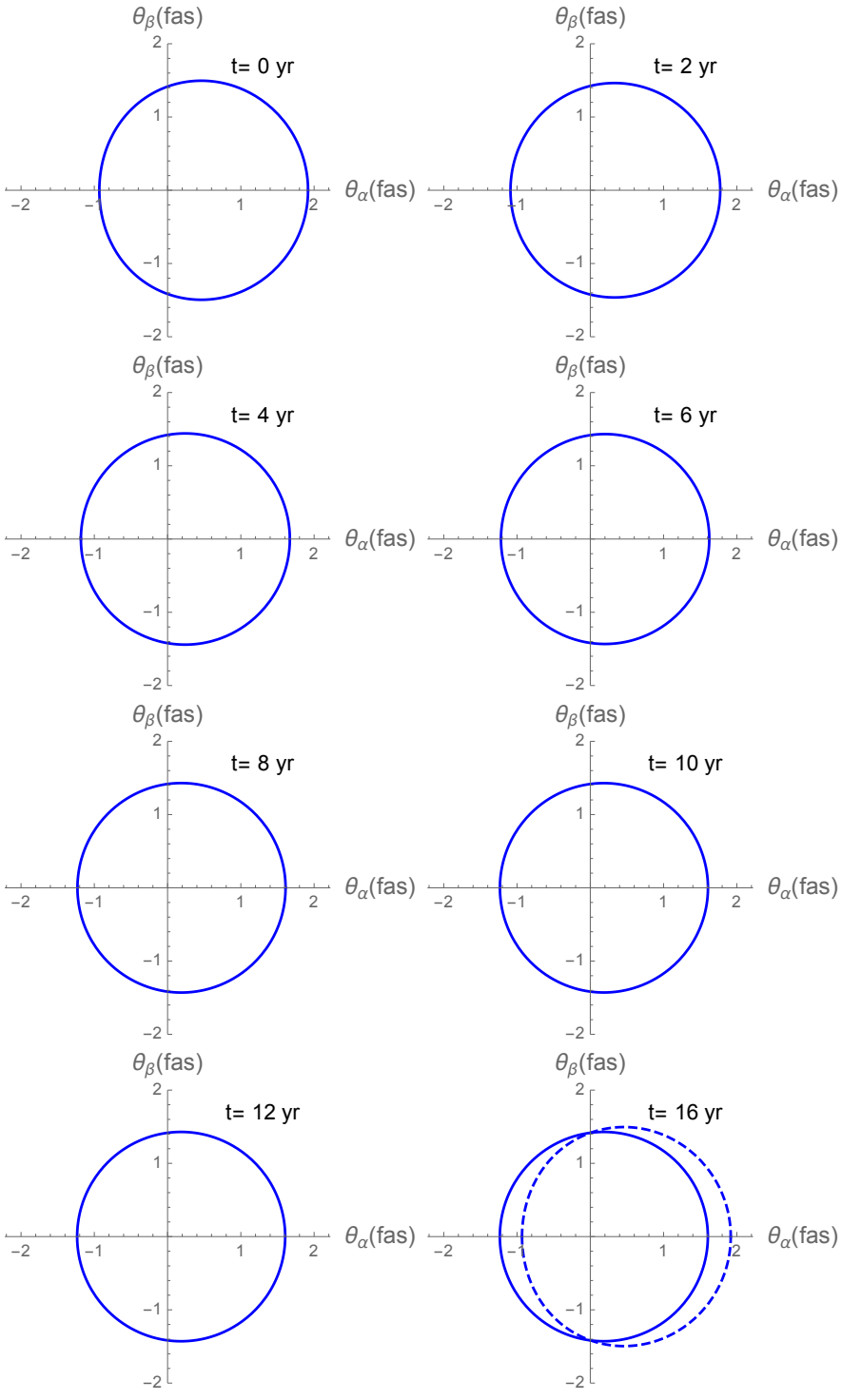

Figure 4.9: Observation of the evolution of the shadow diameter with time (in years) for the mentioned black hole. For comparison, in the last plot we have plotted the shadow at $t = 0$ as a dashed line.

Conclusions and outlook

Alongside multi-messenger astronomy and, specifically, gravitational wave detectors, superradiance has probed to be one of the most promising mechansisms to study ultralight particles. A lot of work has been done towards the gravitational wave detection of such a phenomena ([6], [8], [9], [20], [35]), but little has been done regarding the electromagnetic spectrum ([36]).

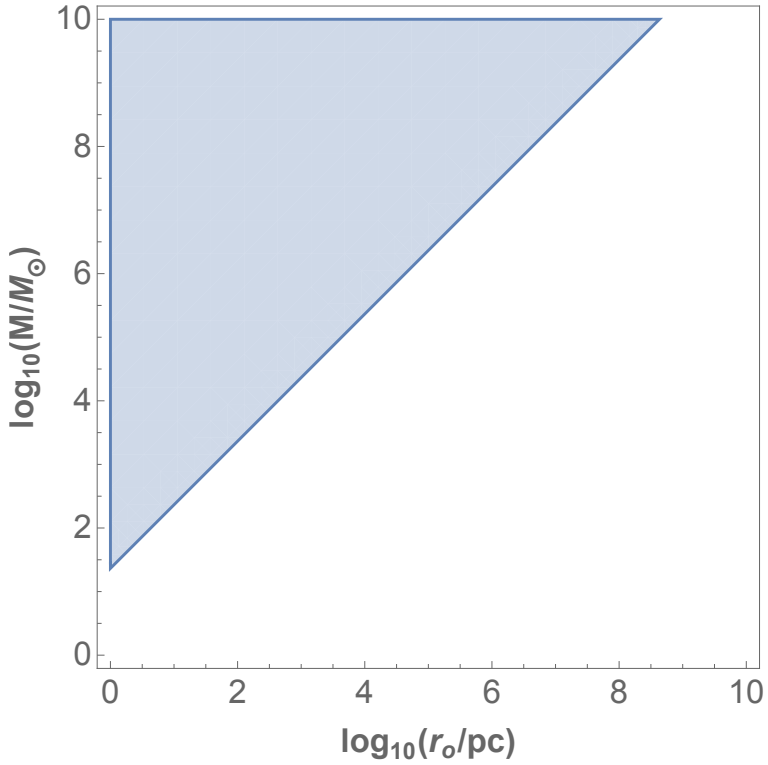

Figure 4.10: Parameter space of mass of the black hole (in solar mass) vs the black hole distance (in parsecs) satisfying $d_{sh} > 10^{-11}$as, being d_{sh} the shadow angular diameter. For this plot we have assumed an equatorial observer and an extremal black hole spin since is the case of maximum change of the angular diameter.

In this master thesis we have reviewed and studied the Gravatom and its evolution, where we have seen that superradiant instability can be potentially observable due to feasible astronomical time-scales. We have also studied gravitational lensing, focusing on the shadow of a Kerr black hole and seen that it shows sensitivity to the black hole spin and mass. In an attempt to measure the ultralight boson mass, we have modelized the spin evolution of the black hole due to the superradiant instability and provided a fitted formula. Furthermore, we have also studied the shadow of the black hole in more detail, providing numerical calculations of the shadow angular diameter and also giving a fitted formula for an equatorial observer valid

for any mass and spin. Combining the different equations and observable parameters allow us to find the energy mode and initial mass of the ultralight boson cloud and finally solve for the mass of the boson.

We have also given an idea of how to use this method alongside gravitational waves not only as a cross-check but also as the only available method for certain complex field configurations, showing an example with one of the gravitational wave detections. Furthermore, we see that the superradiant instablity leaves a characteristic imprint in the shadow diameter, making it distinguishable from other possible spindown processes. Figure 4.10 shows the parameter space such that the angular resolution of the shadow is larger or of the order of micro-arcseconds, therefore it would be worth to study the dynamical time-scales and the possible observation with current telescopes like the Event Horizon Telescope (EHT).

Further studies in this line of research would include taking into account accretion and the effects of the spindown in the magnification and caustics of the Kerr black hole. Numerical computations in the quasi-adiabatic regime suggest that accretion play a very important role [23] in the development of the instability. Studying the spin evolution of supermassive black holes with accretion disks can lead to potentially observational signatures within the angular resolution of the EHT. During this master thesis we tried to reproduce the computations of ref. [26] in order to also relate the effects of the magnification and position of relativistic images to the spin of the black hole but we did not include the results due to complications and discrepances with the code. Also, it would be very interesting to construct the whole observation picture taking into account the mentioned factors and the study of ref. [36], where in the case of the axion being the ultralight boson, they study the effects of the weak axion-photon coupling in the polarization of light within the gravitational lensing effect. On the other hand, given the interest in black hole binaries triggered by the gravitational wave detections [9], it would be of interest to study the gravitational lensing effect of a binary including a Gravatom.

Acknowledgements

I am very grateful to Helvi Witek for the support and guidance during the last years. Also, to my supervisor Stefan Vandoren for the discussions, motivation and guidance. Finally, thank my family for the constant support and inspiration and to my friends and fellow students for making of Utrecht my home, specially Jordi, Claire, Alina and Leona.

Appendix A

Mathematics preliminaries for Chapter 1

A.1 Spheroidal wave function

A.1.1 Spherical case

When solving the Helmholtz equation in spherical coordinates

$$\left(\nabla^2 + k^2\right)\psi = 0 \ , \tag{A.1}$$

and using separation of variables $\psi = R(r)\Theta(\theta)\Phi(\varphi)$ we obtain the associated Legendre equation (via the change $x = \cos(\theta)$ and $\Theta(\theta) = y(x)$)

$$\frac{\mathrm{d}}{\mathrm{d}x}\left[\left(1-x^2\right)\frac{\mathrm{d}}{\mathrm{d}x}y(x)\right] + \left(Q - \frac{m^2}{1-x^2}\right)y(x) = 0 \ . \tag{A.2}$$

Here m^2 is the angular separation constant between the φ and the r and θ dependence such that

$$\frac{\mathrm{d}^2\Phi}{\mathrm{d}\varphi^2} = -m^2\Phi \ , \tag{A.3}$$

and Q is the separation constant between the r and θ dependence. The solution to this equation are the associated Legendre polynomials

$$y(x) = P_l^m(x) = (-1)^l(1-x^2)^{m/2}\left(\frac{\mathrm{d}}{\mathrm{d}x}\right)^m P_l(x) \ , \tag{A.4}$$

with

$$P_l(x) = \frac{1}{2^l l!}\left(\frac{\mathrm{d}}{\mathrm{d}x}\right)^l (x^2-1)^l \ .$$

Then the solution reads, after normalization,

$$\Psi_{nml} = R_n(r)Y_{lm}(\theta,\varphi) \ . \tag{A.5}$$

With $R_n(r)$ the solution to the Bessel differential equation and Y_{lm} the spherical harmonics defined by

$$Y_{lm}(\theta,\varphi) = \left[\frac{2l+1}{4\pi}\frac{(l-m)!}{(l+m)!}\right]^{1/2} P_l^m(\cos\theta)e^{im\varphi} \ .$$

where the overall factor comes from demanding $\langle Y_{l,m}|Y_{l',m'}\rangle = \delta_{l,l'}\delta_{m,m'}$ using the property $\langle P_l^m|P_{l'}^m\rangle = \frac{(l+m)!}{(l-m)!}\frac{2}{2l+1}\delta_{l,l'}$.

A.1.2 Spheroidal case

The spheroidal coordinate system (ξ, η, ϕ) distinguish between a prolate or oblate configuration and are depicted in fig. A.1. Here, d is the interfocal distance and η and ϕ are parameters describing the spheroidicity. The relation between prolate and oblate and Cartesian coordinates is given in ref. [37] and shown in Table A.1.

Prolate	Oblate
$x = \frac{d}{2}\sqrt{(1-\eta^2)(\xi^2-1)}\cos(\phi)$	$x = \frac{d}{2}\sqrt{(1-\eta^2)(\xi^2+1)}\cos(\phi)$
$y = \frac{d}{2}\sqrt{(1-\eta^2)(\xi^2-1)}\sin(\phi)$	$y = \frac{d}{2}\sqrt{(1-\eta^2)(\xi^2+1)}\sin(\phi)$
$z = \frac{d}{2}\xi\eta,$	$z = \frac{d}{2}\xi\eta,$
$\eta \in [-1,1],\ \xi \in [1,\infty),\ \phi \in [0,2\pi]$	$\eta \in [-1,1],\ \xi \in [0,\infty),\ \phi \in [0,2\pi]$

Table A.1: Prolate and Oblate to Cartesian coordinates relations.

In order to change from the prolate to the oblate coordinate system one has to do the change $\xi \to i\xi$ and $d \to -id$. For simplicity we will write the equations in the prolate spheroidal coordinates.

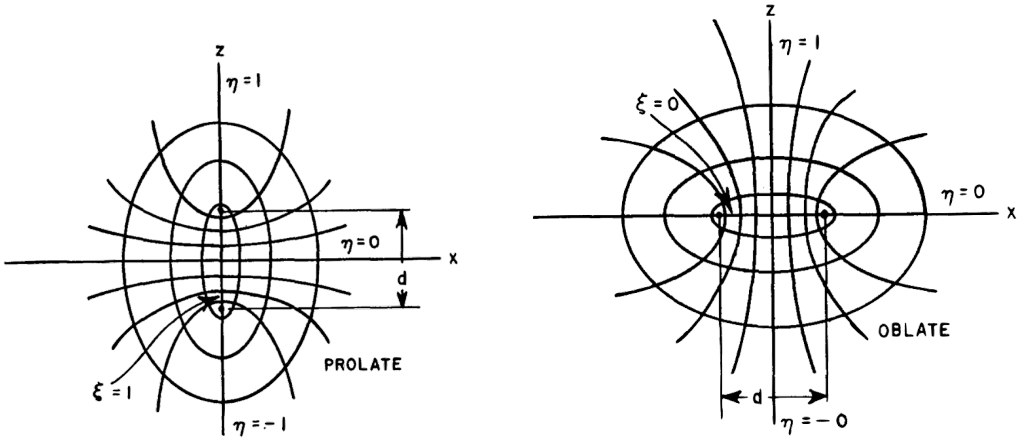

(a) Prolate **(b)** Oblate

Figure A.1: Prolate and oblate coordinate systems. Ilustrations taken from [38]

.

Analogously to the spherical case, in order to solve eq. (A.1) one does the variable separation

$$\Psi_{ml} = R_{ml}(c,\xi)S_{ml}(c,\eta)\phi_m(\varphi)\ , \tag{A.6}$$

such that the equation for the angular function $S_{mn}(c,\eta)$ reads

$$\frac{\mathrm{d}}{\mathrm{d}\eta}\left[(1-\eta^2)\frac{\mathrm{d}}{\mathrm{d}\eta}S_{ml}(c,\eta)\right] + \left(\lambda_{ml}(c) - c^2\eta^2 - \frac{m^2}{1-\eta^2}\right)S_{ml}(c,\eta) = 0\ , \tag{A.7}$$

with $c \equiv \frac{1}{2}kd$. We see that this equation is very similar to eq. (A.2) but now $Q = Q(\eta)$. If $c = 0$ then we recover the spherical case and the solution is given in terms of the associated Legendre

polynomials. In order to solve the differential equation one does the following expansion for the spheroidal functions of the first kind

$$S_{ml}(c,\eta) = \sum_{r=0,1}^{\infty} d_r^{ml}(c) P_{m+r}^m(\eta) \ , \tag{A.8}$$

where the sum goes over all even values of r if $l-m$ is even and over all odd values of r if $l-m$ is odd. One can easily see that $\lambda_{ml}(0) = l(l+1)$ since the differential equation reduces to the one obtained for the spherical case.

A.2 Horizon angular velocity

Let us consider a photon emmited in the φ direction at some radius r in the equatorial plane. Considering its initial momentum to don't have r or θ components, the null trajectory condition is

$$ds^2 = 0 = g_{tt}dt^2 + g_{t\varphi}dtd\varphi + g_{\varphi\varphi}d\varphi^2 \ ,$$

such that

$$\frac{d\varphi}{dt} = -\frac{g_{t\varphi}}{2g_{\varphi\varphi}} \pm \sqrt{\frac{1}{4}\left(\frac{g_{t\varphi}}{g_{\varphi\varphi}}\right)^2 - \frac{g_{tt}}{g_{\varphi\varphi}}} \ .$$

In the stationary limit surface $g_{tt} = 0$ we have two solutions,

$$\left(\frac{d\varphi}{dt}\right)_+ = 0 \ , \quad \left(\frac{d\varphi}{dt}\right)_- = \frac{a}{2G^2M^2 + a^2} \ .$$

The first solution corresponds to a photon moving in the counter-rotating direction and the second one corresponds to a co-rotating photon. Massive particles move more slow than photons and get dragged along with the black hole rotation once crossed the stationary limit surface (defined by $K^\mu K_\mu = 0$, where K_μ is a killing vector). The event horizon angular velocity Ω_H is defined as the minimum angular velocity of a particle at the horizon. Hence

$$\Omega_H \equiv \left(\frac{d\varphi}{dt}\right)_- (r_+) = \frac{a}{r_+^2 + a^2} = \frac{a}{2Mr_+}. \tag{A.9}$$

A.3 Whittaker equation

E.T. Whittaker [39] proposed a function from which Parabolic Cylinder Functions, the Error Function, the Incomplete Gamma Functions, the Logarithm Integral and Cosine Integral could be derived from. This function is called Whittaker function,

$$W_{k,m}(z) = \frac{\Gamma(k+\frac{1}{2}-m)}{2\pi} e^{-1/2z+1/2i\pi} z^k \int (-t)^{-k-1/2+m}\left(1+\frac{t}{z}\right)^{k-1/2+m} e^{-t}dt \ ,$$

where the path of integration begins at $t = +\infty$, and after encircling the point $t = 0$ in the counter-clockwise direction returns to $t = +\infty$ again. The t-plane is supposed to be dissected by a cut from $t = 0$ to $t = +\infty$.

Writing

$$v = \int (-t)^{-k-1/2+m}\left(1+\frac{t}{z}\right)^{k-1/2+m} e^{-t}dt \ ,$$

we have

$$\frac{d^2v}{dz^2} + \left(\frac{2k}{z} - 1\right)\frac{dv}{dz} + \frac{\frac{1}{4} - m^2 + k(k-1)}{z^2}v = 0 \ .$$

From the definition of $W_{k,m}(z)$ we have $W_{k,m}(z) = Ce^{-1/2z}z^k v$ with C being a constant. Substituting v in terms of $W_{k,m}(z)$ we get

$$\frac{d^2W}{dz^2} + \left(-\frac{1}{4} + \frac{k}{z} + \frac{\frac{1}{4} - m^2}{z^2}\right) W = 0 \ ,$$

which is the Whittaker differential equation.

A.3.1 Relation to confluent hypergeometric functions

Whittaker equation is obtained from Kummer equation

$$z\frac{\mathrm{d}^2w}{\mathrm{d}z^2} + (b-z)\frac{\mathrm{d}w}{\mathrm{d}z} - aw = 0 \ ,$$

by the following change of variables and substitutions

$$w_{\mathrm{Whit}}(z) = e^{-\frac{1}{2}z}z^{1/2+m}w_{\mathrm{Kumm}}(z) \ , \quad k = \frac{1}{2}b - a \ , \quad m = \frac{1}{2}b - \frac{1}{2} \ .$$

The solutions to the Kummer equation are

$$M\left(a,b,z\right) = \sum_{s=0}^{\infty}\frac{(a)_s}{(b)_s s!}z^s = 1 + \frac{a}{b}z + \frac{a(a+1)}{b(b+1)2!}z^2 + \cdots \ , \tag{A.10a}$$

$$U(a,b,z) = \frac{\pi}{\sin(b\pi)}\left[\frac{M(a,b,z)}{\Gamma(1+a-b)\Gamma(b)} - \frac{z^{1-b}M(a+1-b,2-b,z)}{\Gamma(a)\Gamma(-b)}\right] \ . \tag{A.10b}$$

These are also called confluent hypergeometric functions of first and second kind, respectively. The function $U(a,b,z)$ is also called Tricomi function. Alternatively one can define the Whittaker functions of the first and second kind

$$M_{k,m}(z) = e^{-\frac{z}{2}}z^{\frac{1}{2}+m}M(\frac{1}{2}+m-k,1+2m,z) \ , \tag{A.11a}$$

$$W_{k,m}(z) = e^{-\frac{z}{2}}z^{\frac{1}{2}+m}U(\frac{1}{2}+m-k,1+2m,z) \ . \tag{A.11b}$$

In particular the second solution is the one of interest in this work. This is due to the behavior of the Kummer functions at infinity: the function $M(a,b,z)$ is not suitable for an assymptotic treatment at large z (this can be seen looking, e.g., at the integral representation [40]).This is, in fact, the motivation that lead Whittaker to define the second Whittaker function $W_{k,m}(z)$.

One of the most famous problems solved in terms of the hypergeometric functions is the Schrödinger equation for the hydrogen atom. Depending on the literature one can see the use of $M_{k,m}$ or $W_{k,m}$ without any specific criteria. These two functions regarding this problem are equivalent in the sense that imposing boundary conditions makes them behave, as it should be, equally. In particular one sets the first parameter, a, to be a non-negative integer. In the case of the Whittaker function of the first kind $M_{k,m}(a,b,z)$ this is done for the function to behave as a polynomial for large values of z and then solve the problem of the behavior at large values of z. On the other hand, for the Whittaker function of the second kind $W_{k,m}(a,b,z)$, as we do in this work, one imposes this condition in order to have a regular solution at small values of z.

A.4 Transformation to hypergeometric differential equation

Any homogeneous linear differential equation of the second order with at most three distinct regular singularities, in the extended plane can be transformed into the hypergeometric equation,

$$z(1-z)\frac{\mathrm{d}^2w}{\mathrm{d}z^2} + (c-(a+b+1)z)\frac{\mathrm{d}w}{\mathrm{d}z} - abw = 0 \ . \tag{A.12}$$

Let's see how. The most general form of this kind of equations is [41]

$$\frac{\mathrm{d}^2 w}{\mathrm{d}z^2} + \left(\frac{1-a_1-a_2}{z-\alpha} + \frac{1-b_1-b_2}{z-\beta} + \frac{1-c_1-c_2}{z-\gamma} \right) \frac{\mathrm{d}w}{\mathrm{d}z} + \left(\frac{(\alpha-\beta)(\alpha-\gamma)a_1 a_2}{z-\alpha} + \frac{(\beta-\alpha)(\beta-\gamma)b_1 b_2}{z-\beta} + \frac{(\gamma-\alpha)(\gamma-\beta)c_1 c_2}{z-\gamma} \right) \frac{w}{(z-\alpha)(z-\beta)(z-\gamma)} = 0 \ ,$$

with $a_1 + a_2 + b_1 + b_2 + c_1 + c_2 = 1$. The complete set of solutions is denoted by Riemann's P-symbol

$$w = P \left\{ \begin{matrix} \alpha & \beta & \gamma & \\ a_1 & b_1 & c_1 & ; z \\ a_2 & b_2 & c_2 & \end{matrix} \right\} .$$

Eq.(A.12) is then expressed as

$$w = P \left\{ \begin{matrix} 0 & 1 & \infty & \\ 0 & 0 & a & ; z \\ 1-c & c-a-b & b & \end{matrix} \right\} .$$

By means of a conformal map $t = (kz+\lambda)/(\mu z+\nu)$ one can map any two sets of distinct points into each other and therefore

$$P \left\{ \begin{matrix} \alpha & \beta & \gamma & \\ a_1 & b_1 & c_1 & ; z \\ a_2 & b_2 & c_2 & \end{matrix} \right\} = P \left\{ \begin{matrix} \widetilde{\alpha} & \widetilde{\beta} & \widetilde{\gamma} & \\ a_1 & b_1 & c_1 & ; t \\ a_2 & b_2 & c_2 & \end{matrix} \right\} .$$

The reduction to the hypergeometric differential equation is given by

$$P \left\{ \begin{matrix} \alpha & \beta & \gamma & \\ a_1 & b_1 & c_1 & ; z \\ a_2 & b_2 & c_2 & \end{matrix} \right\} = \left(\frac{z-\alpha}{z-\gamma} \right)^{a_1} \left(\frac{z-\beta}{z-\gamma} \right)^{b_1} P \left\{ \begin{matrix} 0 & 1 & \infty & \\ 0 & 0 & a_1+b_1+c_1 & ; \dfrac{(z-\alpha)(\beta-\gamma)}{(z-\gamma)(\beta-\alpha)} \\ a_2-a_1 & b_2-b_1 & a_1+b_1+c_2 & \end{matrix} \right\} .$$

One can obtain the Kummer equation as a limiting case of the hypergeometric differential equation

$$w = \lim_{b\to\infty} P \left\{ \begin{matrix} 0 & 1 & \infty & \\ 0 & 0 & a & ; z/b \\ 1-c & c-a-b & b & \end{matrix} \right\} ,$$

and subsequently replacing the symbol c by b.

Appendix B

Far region approximation

In order to check the approximation one can plot the coefficients of eq. (1.6). Let us define the following functions

$$f(r) \equiv -\kappa^2 r^4 + 2M\mu^2 r^3 - 2M^2 r^2 \kappa^2 - r^2(M^2\omega^2 + \lambda) + 2Mr(\lambda - 2M\omega m + M^2\omega^2) + M^2(m^2 - \lambda) \ ,$$
$$g(r) \equiv -\kappa^2 r^4 + 2M\mu^2 r^3 - r^2\lambda \ ,$$

with $\lambda = l(l+1)$, such that eq. (1.6) reads

$$\Delta_M \partial_r(\Delta_M \partial_r)R(r) + f(r)R(r) = 0 \ ,$$

where $f(r)$ and Δ_M contain the terms of eq. (1.6) with the substitution $a = M$, since it provides an upper boundary. $g(r)$ is $f(r)$ in the large distance and small mass coupling limit. If the approximation is valid, the assimptotic behavior of both functions should be the same. In order to see this clearly we can plot both functions in the regime at which the approximations are valid. As an example let us take $\mu = 1/1001, \omega = 1/1000 \sim \mu$, such that the range of validity will be until $r = 1/\omega = 1000$ where we have set $M = 1$ for simplicity. If we plot both functions we get an overlapping (fig. B.1a), so in order to get a better clue of the behavior we plot the ratio between them $f(r)/g(r)$ (fig. B.1b). We see that the linear term $2Mr\lambda$ is supressed for large distances and therefore, for small mass coupling and $r \gg r_+ + M$, the approximation $f(r) \sim g(r)$ is valid.

So far we have only justified the function $g(r)$ but, what about Δ_M? Explicitly, $\Delta_M = r^2 - 2Mr + M^2$, such that the first term of the differential equation reads, after the corresponding expansion,

$$(r^4 - 4Mr^3 + 6M^2r^2 - 4M^3r + M^4)\partial_r^2 + 2(r^3 - 3Mr^2 + M^2r + 2M^2r - M^3)\partial_r.$$

The idea is to keep the dominant term in each parenthesis. For doing so, we will follow the same strategy as before and look at the behavior of the functions. Again, looking at the ratio between the function and the approximation we see that indeed the approximation is valid.

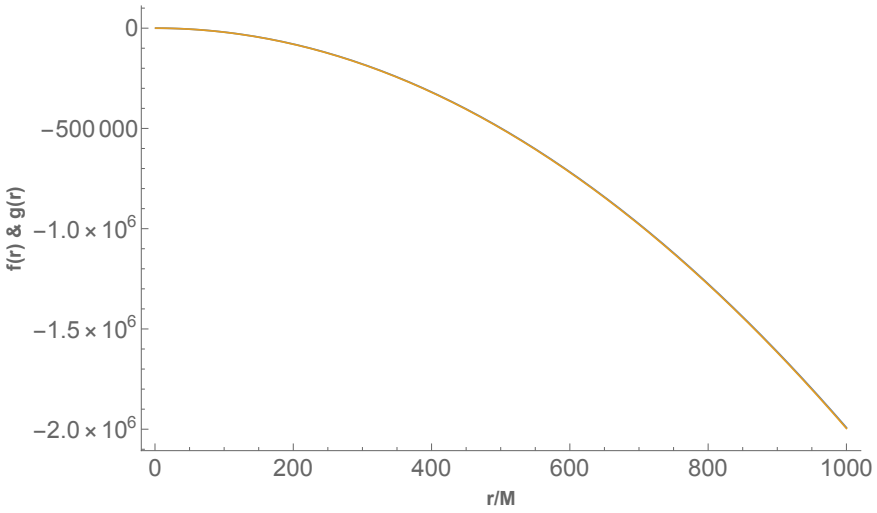

(a) Plot of the functions $f(r)$ (blue) and $g(r)$ (orange). Due to the overlapping one cannot distinguish them.

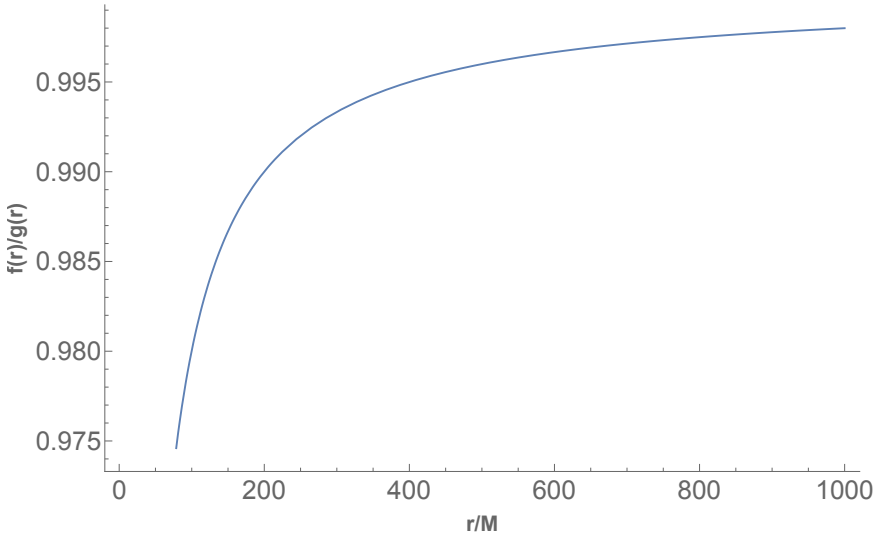

(b) Plot of the rate $f(r)/g(r)$. At large values of r we see that the ratio approaches 1. Even if we are not looking at very large distances, the approximation is good enough.

Figure B.1: Numerical example of the assymptotic behavior of the functions $f(r)$ and $g(r)$.

.

Appendix C

Computations of gamma functions

Here we present the explicit calculations done for the different gamma functions. We use the property $z\Gamma(z) = \Gamma(z+1)$ for every complex value z.

$$\Gamma(2l+1) = (2l)!$$

$$\Gamma(l+1) = l!$$

$$\Gamma(-l) = \frac{\Gamma(-l+1)}{-l} = \frac{\Gamma(-l+2)}{(-l)(-l+1)} = \cdots = \frac{\Gamma(1)}{(-1)^l l!}$$

$$\Gamma(1+l-2i\varpi) = (l-2i\varpi)\Gamma(l-2i\varpi) = (l-2i\varpi)(l-2i\varpi-1)\Gamma(l-2i\varpi-1) =$$
$$= \cdots = \Gamma(1-2i\varpi)\prod_{k=1}^{l}(k-2i\varpi)$$

$$\Gamma(l-2i\varpi) = \frac{\Gamma(-l-2i\varpi)}{-l-2i\varpi} = \frac{\Gamma(-l-2i\varpi+2)}{(-l-2i\varpi)(-l-2i\varpi+1)} = \cdots = \frac{\Gamma(-2i\varpi)}{(-1)^l\prod_{k=1}^{l}(k+2i\varpi)} =$$
$$= \frac{\Gamma(1-2i\varpi)}{2i\varpi(-1)^{l+1}\prod_{k=1}^{l}(k+2i\varpi)}$$

$$\frac{\Gamma(-2l-n-1+\delta\nu)}{\Gamma(-n+\delta\nu)} \simeq \frac{\Gamma(-2l-n-1)}{\Gamma(-n+\delta\nu)} = \frac{(-n+\delta\nu)\Gamma(-2l-n)}{(-2l-n-1)\Gamma(-n+\delta\nu+1)} =$$
$$= \frac{(-n+\delta\nu)(-n+\delta\nu+1)\Gamma(-2l-n+1)}{(-2l-n-1)(-2l-n)\Gamma(-n+\delta\nu+2)} =$$
$$= \frac{(-n+\delta\nu)\dots(-1+\delta\nu)(\delta\nu)\Gamma(1)}{(-2l-n-1)\dots(1)\Gamma(1+\delta\nu)} \simeq (-1)^{2l+1}\delta\nu\frac{(n!)}{(2l+n+1)!}$$

Where we have used that $\delta\nu \ll 1$.

Appendix D

Black hole spin evolution formula derivation

In order to obtain equations (4.5) and (4.7) we first have to study the spin evolution and see if we can apply any approximation to solve the problem. First, for comparison with the literature, we will treat the case of a black hole of initial mass $M_0 = 10^7 M_\odot$ and initial spin $J_0/M_0^2 = 0.8$ for an ultralight boson of mass $\mu = 1 \times 10^{-18}$eV (Case I from now on). Later, we will see the familiar case of the $6M_\odot$ black hole with the same initial spin and a boson mass of $\mu = 7 \times 10^{-12}$eV (Case II from now on). We will start presenting the results and then we will derive the fitted formulas (or *ansatz*). The numerical solution and the fitted formulas for

Case	M_0	μ	J_0/M_0^2	l
I	$10^7 M_\odot$	10^{-18}eV	0.8	1
II	$6M_\odot$	7×10^{-12}eV	0.8	2

Table D.1: Summary of the different initial conditions for the spin evolution.

case I and II are plotted in fig. D.1. For clearness we have omitted the plots corresponding to the mass and spin of the cloud.

D.1 Seeds

As said in sec. 4.1, the numerical solution corresponds to solving the system of coupled differential equations (4.1) for which one also has to provide a seed for the initial mass of the cloud. Here we will treat the case of a seed $0.5M_0 > M_{c,0} \geq 0.01M_0$, in particular the values $M_{c,0} = 0.025M_0$ (astrophysical seed) and $M_{c,0} = 0.3M_0$ (massive seed). Since we have different behaviors for different seeds, we will propose a different ansatz for each seed and use the differential equations to compute the coefficients.

D.1.1 Massive seed

For the massive seed, noticing the exponential behavior of the numerical solution, we will use the following ansatz for the spin (or equivalently angular momentum) evolution

$$J(t) = Ae^{-\gamma t} + B \ . \tag{D.1}$$

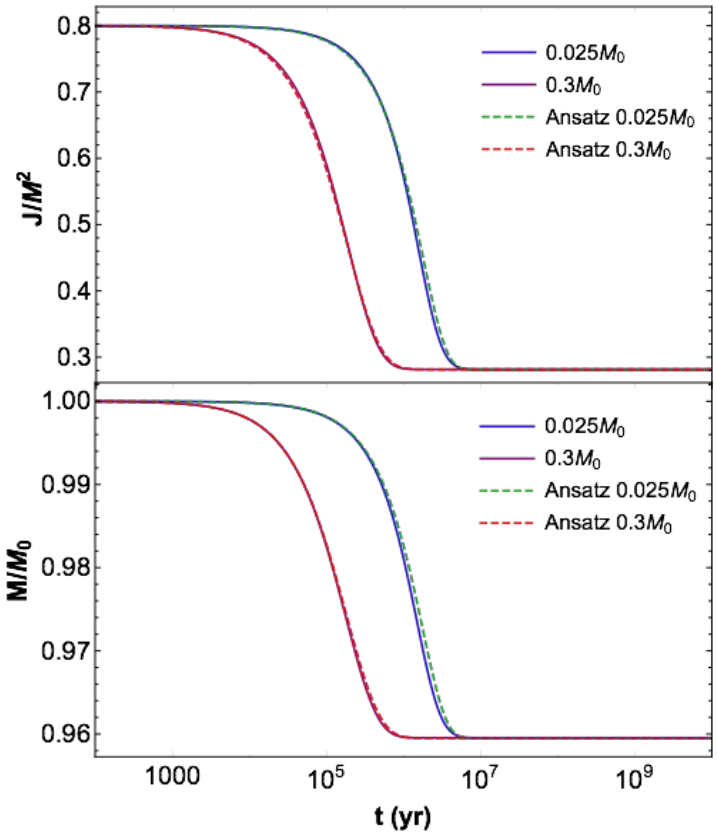

(a) Case I

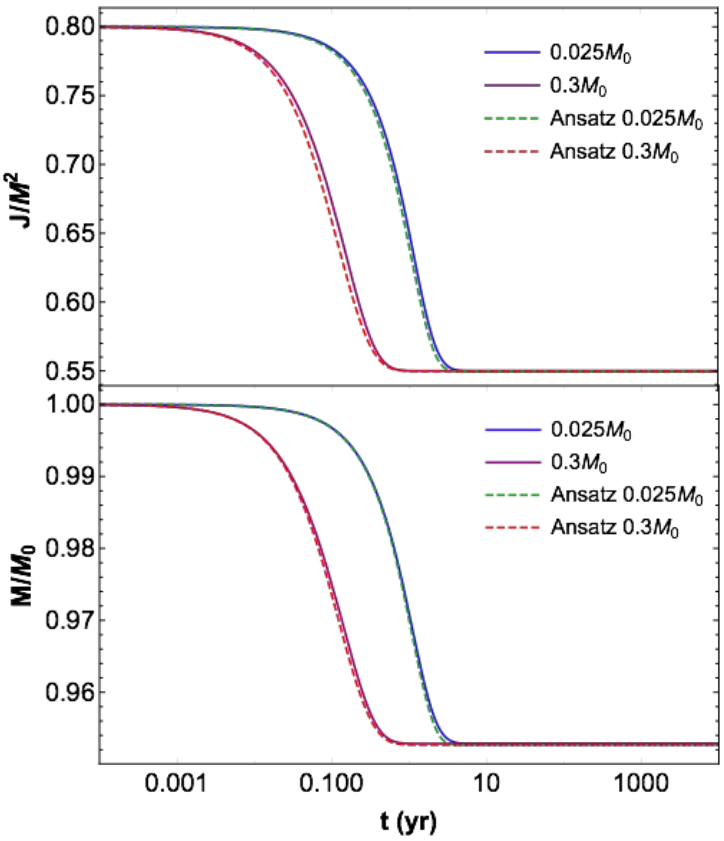

(b) Case II

Figure D.1: Spin evolution for different seeds. The dashed lines correspond to the respective ansatz or fitted formulas

Applying initial conditions: $J(0) \equiv J_0$ and $J(t \to \infty) = J_f$, yields

$$J(t) = (J_0 - J_f)e^{-\gamma t} + J_f \ .$$

In order to compute the exponent γ we will use the spin differential equation,

$$\frac{dJ}{dt} = -\frac{2l}{\mu}\Gamma_{nlm}M_c \ ,$$

and take the value at $t = 0$,

$$\left.\frac{dJ}{dt}\right|_{t=0} = -\frac{2l}{\mu}\Gamma_{nlm,0}M_{c,0} \ ,$$

such that using the ansatz and solving for γ yields

$$\gamma = \frac{2l\Gamma_{nlm,0}M_{c,0}}{\mu(J_0 - J_f)} \ . \tag{D.2}$$

Finally, the ansatz reads

$$J(t) = (J_0 - J_f)\exp\left(-\frac{2l\Gamma_{nlm,0}M_{c,0}}{\mu(J_0 - J_f)}\ t\right) + J_f \ . \tag{D.3}$$

It is worth to mention that when computing the dimensionless spin $\chi \equiv J/M^2$ we should take into account the final and initial mass of the black hole,

$$\chi(t) = \left(\frac{J_0}{M_0^2} - \frac{J_f}{M_f^2}\right)\exp\left(-\frac{2l\Gamma_{nlm,0}M_{c,0}}{\mu(J_0 - J_f)}\ t\right) + \frac{J_f}{M_f^2} \ . \tag{D.4}$$

where the final mass is given by (4.15)[1]. Analogously one can also repeat the same procedure for the mass of the black hole, the mass of the cloud and the spin of the cloud. In general, the fitted formula for the parameter $p(t)$ reads

$$p(t) = (p_0 - p_f)e^{-\gamma t} + p_f \ , \qquad \gamma = \left.\frac{dp}{dt}\right|_{t=0}\frac{1}{p_0 - p_f} \ . \tag{D.5}$$

D.1.2 Astrophysical seed

The ansatz corresponding to the massive seed does not describe properly the behavior of the astrophysical seed. This is because for this case the change is faster such that we have to take into account one more order in the time evolution. For this case the ansatz is given by

$$J(t) = Ae^{-\gamma t - \beta t^2} + B \ . \tag{D.6}$$

where the coefficients A, B, γ are the same as for the massive seed. In order to compute the β coefficient we need an extra condition. This condition will be the time t_* at which all the parameters envolved in the evolution are half of their total value. We can estimate this time by looking at the derivative,

$$\left.\frac{dJ}{dt}\right|_{t=t_*} = -\frac{2l}{\mu}\Gamma_{nlm,*}M_{c,*} \sim \frac{\frac{J_f+J_0}{2} - J_0}{t_*} \ , \tag{D.7}$$

[1] Of course we mention this for the interested reader that wants to use this expression as an alternative for the numerical calculation. Notice that this can only be used for cases when the mass of the cloud is known such that the final mass of the black hole can be computed. In order to do so one can use eq. (2.8),

$$M_0 - M_f = M_0\frac{\alpha_0}{l}\chi_0 - M_f\frac{4M_f^2\mu^2}{l^2 + 4M_f^2\mu^2} \ ,$$

and solve for M_f, which results in eq, (4.15)

and, from the numerical computation, using that

$$M_{c,*} = \frac{M_{c,f} + M_{c,0}}{2} \ , \qquad \Gamma_{nlm,*} = \frac{\Gamma_{nlm,0}}{2} \ , \tag{D.8}$$

yields

$$t_* = \frac{J_0 - J_f}{M_{c,f} + M_{c,0}} \frac{\mu}{l \ \Gamma_{nlm,0}} = \frac{2}{\gamma} \frac{M_{c,0}}{M_{c,f} + M_{c,0}} \ . \tag{D.9}$$

Now the extra condition is given by

$$J(t_*) = \frac{J_f + J_0}{2} = (J_0 - J_f) e^{-\gamma t_* - \beta t_*^2} + J_f \ ,$$

such that

$$\beta = \frac{\log(2)}{t_*^2} - \frac{\gamma}{t_*} \ , \tag{D.10}$$

and therefore the ansatz for the astrophysical seed reads

$$J(t) = (J_0 - J_f) \exp\left[- \frac{2 l \Gamma_{nlm,0} M_{c,0}}{\mu (J_0 - J_f)} \ t \right] \exp\left[- \left(\log(2) - \frac{2 l \Gamma_{nlm,0} M_{c,0}}{\mu (J_0 - J_f)} \ t_* \right) \left(\frac{t}{t_*} \right)^2 \right] + J_f \ . \tag{D.11}$$

Again, one can also repeat the same procedure for the mass of the black hole, the mass of the cloud and the spin of the cloud. In general, the fitted formula for the parameter $p(t)$ reads

$$p(t) = (p_0 - p_f) e^{-\gamma t - \beta t^2} + p_f \ , \qquad \gamma = \left. \frac{dp}{dt} \right|_{t=0} \frac{1}{p_0 - p_f}, \qquad \beta = \frac{\log(2)}{t_*^2} - \frac{\gamma}{t_*} \ . \tag{D.12}$$

Appendix E

Black hole shadow power formula derivation

Finding an exact formula of the angular diameter of the black hole shadow for all spins and inclinations is difficult due to the difficulty of finding the maximum approach distance $\bar{r}$ for each inclination. The equation to solve is

$$Q + a^2 \cos^2\theta - L^2 \cot^2\theta = 0 \ , \tag{E.1}$$

where Q and L are determined by equations (3.22), (3.24) and (3.25):

$$\begin{aligned} \alpha &= -\frac{L}{\sin\theta_o} \ , \\ L(\bar{r}) &= \frac{\bar{r}^2(\bar{r}-3M) + a^2(M+\bar{r})}{a(M-\bar{r})} \ , \\ Q(\bar{r}) &= \frac{r^3\left(4a^2M - r(r-3M)^2\right)}{a^2(M-r)^2}. \end{aligned}$$

In order to derive equation (4.10) we have computed the angular diameter numerically for all inclinations. Because for inclinations different from 0 the shadow diameter is similar, we have fixed $\theta_o = \pi/2$ for simplicity. For this orientation, using (E.1) we are able to set $Q = 0$. Since our goal is to find an expression valid for all BH mass and observer distance we have proposed an ansatz and computed each coefficient exactly and analytically, given that we can solve for $a = 0$, $a = 0.5M$ and $a = M$. The ansatz is given by

$$d_{sh}(a) = A + B\left[1 - \left(\frac{a}{M}\right)^2\right]^{\delta} \ , \tag{E.2}$$

where the spin is squared due to the symmetry $a \to -a$ and the power δ is justified by looking at the numerical computation, where we see that the derivative is divergent, therefore indicating that $\delta < 1$. In order to compute the three coefficients we need at least three values of the diameter for different spins. Below we compute these values for the case $a = 0, 0.5M, M$.

Case a=0

For the case $a = 0$ we have to use the respective radial potential with $a = 0$ and rederive the expressions for Q and L. The radial potential read

$$R(r) = r^4 - (r^2 - 2Mr)(Q + L^2) \ . \tag{E.3}$$

Next, we set $Q = 0$ such that the shadow diameter will be given by

$$d_{sh}^{a=0} = \frac{2}{r_o}|\theta_\alpha| = \frac{2|L|}{r_o} \ . \tag{E.4}$$

Using the condition that the photon arrives to the observer $du^r/d\lambda|_{r=\bar{r}} = 0 = u^r|_{r=\bar{r}}$ and solving for L and $\bar{r}$ yields $\bar{r} = 3M$ and $L = \pm 3\sqrt{3}M$. Substituting in (E.4) yields

$$d_{sh}^{a=0} = \frac{6\sqrt{3}M}{r_o} \ , \tag{E.5}$$

which is the familiar expression for the shadow of a Schwarzschild BH found in [27].

Case a=0.5M

For $a = 0.5M$ we have to proceed as in the last case and by means of the radial potential solve for L and $\bar{r}$. For this case the solution is given by

$$L_- = -\frac{M}{2}\left[1 + 6\cos\left(\frac{\pi}{9}\right) - 6\cos\left(\frac{2\pi}{9}\right) + 6\sqrt{3}\sin\left(\frac{\pi}{9}\right) + 6\sqrt{3}\sin\left(\frac{2\pi}{9}\right)\right] \ ,$$
$$L_+ = \frac{M}{2}\left[-1 - 6\cos\left(\frac{\pi}{9}\right) + 6\cos\left(\frac{2\pi}{9}\right) + 6\sqrt{3}\sin\left(\frac{\pi}{9}\right) + 6\sqrt{3}\sin\left(\frac{2\pi}{9}\right)\right] \ ,$$

for $\bar{r}_\pm = M\left(2 + \cos(\pi/9) \pm \sqrt{3}\sin(\pi/9)\right)$ respectively. Hence, the shadow diameter reads

$$d_{sh}^{a=0.5M} = \frac{1}{r_o}\left(|L_-| + |L_+|\right) = \frac{6\sqrt{3}M}{r_o}\left[\sin\left(\frac{\pi}{9}\right) + \sin\left(\frac{2\pi}{9}\right)\right] \equiv \frac{6\sqrt{3}M}{r_o}S \tag{E.6}$$

where in the last step we have defined $S \equiv \sin\left(\frac{\pi}{9}\right) + \sin\left(\frac{2\pi}{9}\right)$.

Case a=M

For the case $a = M$ we have to proceed in the same way as in the case $a = 0.5M$, i.e. solving for L and $\bar{r}$ for the fixed spin. The solutions are $L_+ = 2M$ for $\bar{r}_- = M$ and $L_- = -7M$ for $\bar{r}_+ = 4M$. Therefore

$$d_{sh}^{a=M} = \frac{1}{r_o}\left(|L_-| + |L_+|\right) = \frac{9M}{r_o} \ . \tag{E.7}$$

E.0.1 Finding the coefficients

Given the shadow diameters d_0, $d_{M/2}$ and d_M for $a = 0$, $a = 0.5M$ and $a = M$ respectively, the coefficients of the ansatz $d_{sh}(a) = A + B\left[1 - (a/M)^2\right]^\delta$ read

$$A = d_M = \frac{9M}{r_o} \ , \tag{E.8}$$

$$B = d_0 - A = d_0 - d_M = \frac{3M}{r_o}\left(2\sqrt{3} - 3\right) \ , \tag{E.9}$$

$$\delta = \frac{\log\left(\frac{d_0 - d_M}{d_{M/2} - d_M}\right)}{\log(4/3)} = \frac{\log\left(\frac{2\sqrt{3}-3}{2\sqrt{3}S-3}\right)}{\log(4/3)} \ . \tag{E.10}$$

with $S \equiv \sin\left(\frac{\pi}{9}\right) + \sin\left(\frac{2\pi}{9}\right)$ and in the last step we have substituted the values of the shadow diameters computed above. Finally, the expression for the angular shadow for an observer at $\theta_o = \pi/2$ read

$$d_{sh} = \frac{3M}{r_o}\left\{3 + (2\sqrt{3} - 3)\left[1 - \left(\frac{a}{M}\right)^2\right]^\delta\right\} \ . \tag{E.11}$$

Bibliography

[1] B. P. Abbott et al. "Observation of Gravitational Waves from a Binary Black Hole Merger". In: *Phys. Rev. Lett.* 116.6 (2016), p. 061102. arXiv: 1602.03837 [gr-qc].

[2] V. Cardoso and P. Pani. "Tidal acceleration of black holes and superradiance". In: *Class. Quant. Grav.* 30 (2013), p. 045011. arXiv: 1205.3184 [gr-qc].

[3] W. H. PRESS and S. A. TEUKOLSKY. "Floating Orbits, Superradiant Scattering and the Black-hole Bomb". In: *Nature* 238.5361 (1972), pp. 211–212.

[4] T. J. Zouros and D. M. Eardley. "Instabilities of massive scalar perturbations of a rotating black hole". In: *Annals of Physics* 118.1 (1979), pp. 139–155.

[5] S. Detweiler. "Klein-Gordon equation and rotating black holes". In: *Phys. Rev. D* 22 (10 Nov. 1980), pp. 2323–2326.

[6] A. Arvanitaki and S. Dubovsky. "Exploring the String Axiverse with Precision Black Hole Physics". In: *Phys. Rev.* D83 (2011), p. 044026. arXiv: 1004.3558 [hep-th].

[7] L. Hui et al. "Ultralight scalars as cosmological dark matter". In: *Phys. Rev.* D95.4 (2017), p. 043541. arXiv: 1610.08297 [astro-ph.CO].

[8] A. Arvanitaki, M. Baryakhtar, and X. Huang. "Discovering the QCD Axion with Black Holes and Gravitational Waves". In: *Phys. Rev.* D91.8 (2015), p. 084011. arXiv: 1411.2263 [hep-ph].

[9] D. Baumann, H. S. Chia, and R. A. Porto. "Probing Ultralight Bosons with Binary Black Holes". In: *Phys. Rev.* D99.4 (2019), p. 044001. arXiv: 1804.03208 [gr-qc].

[10] K. Akiyama et al. "First M87 Event Horizon Telescope Results. I. The Shadow of the Supermassive Black Hole". In: *Astrophys. J.* 875.1 (2019), p. L1.

[11] V. L. Fish, M. Shea, and K. Akiyama. "Imaging Black Holes and Jets with a VLBI Array Including Multiple Space-Based Telescopes". In: *arXiv e-prints*, arXiv:1903.09539 (Mar. 2019), arXiv:1903.09539. arXiv: 1903.09539 [astro-ph.IM].

[12] D. R. Brill et al. "Solution of the Scalar Wave Equation in a Kerr Background by Separation of Variables". In: *Phys. Rev. D* 5 (8 Apr. 1972), pp. 1913–1915.

[13] Abramowitz and Stegun. *Handbook of Mathematical Functions with Formulas, Graphs, and Mathematical Tables*. 10th. Cambridge University Press, Dec. 1972.

[14] J. M. Bardeen, W. H. Press, and S. A. Teukolsky. "Rotating black holes: Locally nonrotating frames, energy extraction, and scalar synchrotron radiation". In: *Astrophys. J.* 178 (1972), p. 347.

[15] J. M. Cohen and B. Kuharetz. "Relativistic hydrogen atom: Wave equation in Whittaker form". In: *Journal of Mathematical Physics* 34.11 (1993), pp. 4964–4974. eprint: https://doi.org/10.1063/1.530422.

[16] V. Cardoso et al. "The Black hole bomb and superradiant instabilities". In: *Phys. Rev.* D70 (2004). [Erratum: Phys. Rev.D70,049903(2004)], p. 044039. arXiv: hep-th/0404096 [hep-th].

[17] H. J. W. George B. Arfken and F. E. Harris. *Mathematical Methods for Physicists. A Comprehensive Guide*. 7th. Elseiver, 2013.

[18] A. Arvanitaki et al. "String Axiverse". In: *Phys. Rev.* D81 (2010), p. 123530. arXiv: 0905.4720 [hep-th].

[19] R. Brito, V. Cardoso, and P. Pani. "Superradiance". In: *Lect. Notes Phys.* 906 (2015), pp.1–237. arXiv: 1501.06570 [gr-qc].

[20] R. Brito et al. "Gravitational wave searches for ultralight bosons with LIGO and LISA". In: *Phys. Rev.* D96.6 (2017), p. 064050. arXiv: 1706.06311 [gr-qc].

[21] J. D. Bekenstein. "Extraction of Energy and Charge from a Black Hole". In: *Phys. Rev. D* 7 (4 Feb. 1973), pp. 949–953.

[22] S. Carroll, S. Carroll, and Addison-Wesley. *Spacetime and Geometry: An Introduction to General Relativity*. Addison Wesley, 2004.

[23] R. Brito, V. Cardoso, and P. Pani. "Black holes as particle detectors: evolution of superradiant instabilities". In: *Class. Quant. Grav.* 32.13 (2015), p. 134001. arXiv: 1411.0686 [gr-qc].

[24] H. Yoshino and H. Kodama. "Gravitational radiation from an axion cloud around a black hole: Superradiant phase". In: *PTEP* 2014 (2014), 043E02. arXiv: 1312.2326 [gr-qc].

[25] S. Weinberg. *GRAVITATION AND COSMOLOGY: PRINCIPLES AND APPLICATIONS OF THE GENERAL THEORY OF RELATIVITY*. Wiley India Pvt. Limited, 2008.

[26] S. E. Vazquez and E. P. Esteban. "Strong field gravitational lensing by a Kerr black hole". In: *Nuovo Cim.* B119 (2004), pp. 489–519. arXiv: gr-qc/0308023 [gr-qc].

[27] V. Bozza. "Gravitational Lensing by Black Holes". In: *Gen. Rel. Grav.* 42 (2010), pp. 2269–2300. arXiv: 0911.2187 [gr-qc].

[28] D. Morin. *Introduction to Classical Mechanics: With Problems and Solutions*. Cambridge University Press, 2008.

[29] B. Carter. "Global Structure of the Kerr Family of Gravitational Fields". In: *Phys. Rev.* 174 (5 Oct. 1968), pp. 1559–1571.

[30] S. R. Dolan. "Instability of the massive Klein-Gordon field on the Kerr spacetime". In: *Phys. Rev.* D76 (2007), p. 084001. arXiv: 0705.2880 [gr-qc].

[31] G. Ficarra, P. Pani, and H. Witek. "Impact of multiple modes on the black-hole superradiant instability". In: *Phys. Rev.* D99.10 (2019), p. 104019. arXiv: 1812.02758 [gr-qc].

[32] I. Bartos and M. Kowalski. *Multimessenger Astronomy*. 2399-2891. IOP Publishing, 2017.

[33] B. P. Abbott et al. "Multi-messenger Observations of a Binary Neutron Star Merger". In: *The Astrophysical Journal* 848.2 (Oct. 2017), p. L12.

[34] B. P. Abbott et al. "GWTC-1: A Gravitational-Wave Transient Catalog of Compact Binary Mergers Observed by LIGO and Virgo during the First and Second Observing Runs". In: (2018). arXiv: 1811.12907 [astro-ph.HE].

[35] M. Isi et al. "Directed searches for gravitational waves from ultralight bosons". In: *Phys. Rev.* D99.8 (2019), p. 084042. arXiv: 1810.03812 [gr-qc].

[36] A. D. Plascencia and A. Urbano. "Black hole superradiance and polarization-dependent bending of light". In: *JCAP* 1804.04 (2018), p. 059. arXiv: 1711.08298 [gr-qc].

[37] W. J. Thompson. "Spheroidal Wave Functions". In: *Computing in Science & Engineering* 1.3 (1999), pp. 84–87. eprint: https://aip.scitation.org/doi/pdf/10.1109/5992.764220.

[38] D. B. Hodge. "Eigenvalues and Eigenfunctions of the Spheroidal Wave Equation". In: *Journal of Mathematical Physics* 11.8 (1970), pp. 2308–2312. eprint: https://doi.org/10.1063/1.1665398.

[39] E. T. Whittaker. "An expression of certain known functions as generalized hypergeometric functions". In: *Bulletin of the American Mathematical Society* 10.3 (1903), pp. 125–134.

[40] Z. Wang and D. Guo. *Special Functions*. EBL-Schweitzer. World Scientific, 1989.

[41] *NIST Digital Library of Mathematical Functions*. http://dlmf.nist.gov/, Release 1.0.20 of 2018-09-15. F. W. J. Olver, A. B. Olde Daalhuis, D. W. Lozier, B. I. Schneider, R. F. Boisvert, C. W. Clark, B. R. Miller and B. V. Saunders, eds.